

AN ABSTRACT OF THE THESIS OF

Joshua R. Motley for the degree of Master of Science in Chemical Engineering presented on May 27, 2016.

Title: Application of Self-Assembled Monolayers to InGaZnO Thin Film Transistors

Abstract approved:

Gregory S. Herman

Investigations on the application of self-assembled monolayers (SAM) to indium gallium zinc oxide (IGZO) thin film transistors (TFT) for fabrication and channel modification are presented. The back channel of IGZO thin film transistors can be modified by the absorption of self-assembled monolayers. The electrical properties of the IGZO exposed back channel are sensitive to surface chemistries and can be tailored using SAMs. Chemistry at the back channel interface alters device performance. The back channel surface sensitivities can be used in applications for chemical sensing TFTs. IGZO TFTs with and without octadecyl phosphonic acid applied to the back channel with varied channel thicknesses (10-50 nm) were examined. TFT parameters, such as, turn-on voltage, hysteresis, mobility, subthreshold swing, and current on/off ratio were evaluated by current-voltage electrical measurements.

The use of electrohydrodynamic ink jet (EHDP) printing as non-contact method for patterning etch resists with sub-10 μm features was demonstrated for fabrication of IGZO TFTs. EHDP uses an electric field to generate ink droplets that can be smaller than the nozzle diameter. EHDP was used for depositing a self-assembled monolayer, n-hexyl phosphonic acid (HPA), and photoresist, SU8, as etch resists for patterning the IGZO TFT channel. Drop on demand printing is accomplished by overlapping of discrete droplets to form the desired feature. The optimal ink formulations and EHDP parameters were determined for each ink. Parameters were optimized for producing the smallest, uniform printed features. Bottom gate IGZO TFTs were fabricated by plasma sputtering IGZO onto a SiO_2/Si substrate. The IGZO TFT channels were patterned by printing HPA or SU8 ink as the etch resist, and using HCl as the etch solution. Indium tin oxide source and drain were deposited over the patterned channel using plasma sputtering. The electrical performance of IGZO TFTs patterned using HPA and SU8 were compared and evaluated using I-V electrical measurements. Drop on demand printing offers a high-speed, low cost route to TFT fabrication and manufacturing. The long narrow channels produced have applications for TFT sensor technologies. EHDP was shown to be capable of printing etch resists for the patterning and fabrication of IGZO TFTs on the scales relevant for digital displays.

©Copyright by Joshua R. Motley
May 27, 2016
All Rights Reserved

Application of Self-Assembled Monolayers to InGaZnO Thin Film Transistors

by
Joshua R. Motley

A THESIS

submitted to

Oregon State University

in partial fulfillment of
the requirements for the
degree of

Master of Science

Presented May 27, 2016
Commencement June 2017

Master of Science thesis of Joshua R. Motley presented on May 27, 2016

APPROVED:

Major Professor, representing Chemical Engineering

Head of the School of Chemical, Biological, and Environmental Engineering

Dean of the Graduate School

I understand that my thesis will become part of the permanent collection of Oregon State University libraries. My signature below authorizes release of my thesis to any reader upon request.

Joshua R. Motley, Author

ACKNOWLEDGEMENTS

I would like to express my deepest gratitude to Dr. Gregory S. Herman for his support and guidance throughout my research. His insights and patience were critical for improving my understanding of semiconductor technologies and research. Without his support I would not have been able to pursue my research interests in thin film transistor fabrication and characterization. His mentorship not only taught me how to critically evaluate experimental data, but also instilled professional values required by future employers.

I would like to thank the graduate students from Dr. Herman's research group for their support and counseling throughout the research and writing process. Their knowledge in experimental design and result presentation was an integral part for my success throughout the program. I would like recognize Dr. Xiaosong Du's involvement and support during my research. Dr. Du's research in sensor technology laid the framework for my research topic. Our discussions involving experimental design and analysis were invaluable to my understanding of semiconductor devices. His technical expertise helped me with the fabrication and characterization of indium gallium zinc oxide thin film transistors. Finally I would like to thank Dr. Rose E. Ruther for inspiring and encouraging me to enter graduate school.

TABLE OF CONTENTS

	<u>Page</u>
Chapter 1: Introduction	1
Next Generation Electronics	1
Thin Film Transistors.....	2
Thin Film Transistor Electrical Properties and Characteristics	6
Indium Gallium Zinc Oxide.....	7
Self-Assembled Monolayers	8
Fabrication of Thin Film Transistors	10
Electrohydrodynamic Ink Jet Printing	13
Chapter 2: Instruments and Techniques.....	15
Semiconductor Parameter Measurements.....	15
Electrohydrodynamic Ink Jet Printer	20
Chapter 3: Self Assembled Monolayers Applied to the Back Channel of IGZO Thin Film Transistors.....	23
Introduction.....	23
Amorphous Oxide Materials and Processing Requirements	25
IGZO Structure & Electron Transport	26
TFT Mobility	28
Subthreshold Voltage Swing.....	29
Sub Bandgap States.....	30
IGZO Instabilities	32
Channel Thickness	33

TABLE OF CONTENTS (Continued)

	<u>Page</u>
Materials and Methods.....	35
Results and Discussion	37
Turn-on Voltage and Hysteresis	38
Subthreshold Swing and Interface Trap Densities.....	41
Field Effect Mobility.....	44
I _{On} /I _{Off} Current Ratio.....	47
Chapter 4: Patterning of IGZO Thin Film Transistors Using Electrohydrodynamic Ink Jet Printing.....	49
Introduction.....	49
Electrohydrodynamic Ink Jet Printing	52
Literature Review.....	55
Electrohydrodynamic Ink Jet Printing (EHDP)	55
Lithography.....	58
Self-Assembled Monolayers.....	59
Materials and Methods.....	59
SU8 Ink Formulation	60
HPA Ink Formulation	60
Printing Etch Resist Inks.....	61
TFT Fabrication	63
TFT Transfer Characteristics	65
Results and Discussion	66

TABLE OF CONTENTS (Continued)

	<u>Page</u>
HPA Patterned IGZO	66
SU8 Patterned IGZO	69
EHDP Patterned IGZO TFT Performance	72
Chapter 5: Future Directions.....	79
Further Studies on ODPA Applied to the Back Channel.....	79
Further Studies for Electrohydrodynamic Ink Jet Printed IGZO TFTs	82
Works Cited	85

LIST OF FIGURES

<u>Figure</u>	<u>Page</u>
Figure 1. Typical bottom gate structure TFT.....	3
Figure 2. a) Phosphonic acid SAM and example oxide surface. b) SAM bound to surface as monodentate.....	9
Figure 3 a) Photoresist spin coated onto substrate. b) Selective radiation exposure using mask. c) Solubility change in photoresist, soluble regions removed using developer. d) pattern to be transferred by photoresist etch remains. e) Exposed regions are etched. f) Photoresist stripped leaving desired pattern in thin film.	11
Figure 4. Digital patterning of a thin film. a) The resist is selectively patterned on the film. b) For photoresist, heat is applied to crosslink and harden the resist. c) Etching solution is used to remove the exposed film. d) The resist is removed leaving the desired pattern.	12
Figure 5. Semiconductor parameter analyzer probe placement on source, drain, and gate electrodes for a TFT. L is the channel length from source to drain. W is the channel width.	15
Figure 6. Typical TFT I-V transfer plot for n-type AOS TFT. The gate voltage is swept and the log I_D of output current is plotted on the right for identifying mobility and subthreshold swing. Square root of I_D is plotted on the right for identification of turn-on voltage.....	17
Figure 7. a) Schematic diagram of EHDP system. b) Image of printing stage, light sources, ground needle, and printing needle.....	20
Figure 8. Voltage bias between the needle and substrate with a square pulse applied at a constant frequency. The bias maintains the Taylor cone at the tip and each pulse ejects a single ink droplet.....	22
Figure 9. a) XRD patterns of deposited amorphous IGZO annealed 400-600 °C. Onset of crystallization is observed at 525 °C. b) Mobility of deposited amorphous IGZO annealed 0-600 °C. “Reprinted from Phys. Stat. Sol., 205 / 8, Nomura et al., Relationship between non-localized tail states and carrier transport in amorphous oxide semiconductor, In–Ga–Zn–O, pg. 1910-1914 Copyright (2008), with permission from John Wiley and Sons.”.	27
Figure 10. Summary of density of states in IGZO films and their relative energy levels. Created using literature data from [79].	31
Figure 11. TFT parameter extraction from 20 nm thick channel IGZO TFT transfer curve. Arrows show the direction of V_G sweep.....	36

LIST OF FIGURES (Continued)

<u>Figure</u>	<u>Page</u>
Figure 13 Transfer curves for 10, 20, 35, and 50 nm IGZO TFTs with and without ODPA. Curves show both the up and down V_G sweeps with $V_D = 0.1$ V.....	38
Figure 12. a) Schematic of experimental IGZO bottom gate TFT structure. b) Experimental IGZO TFT device with ODPA applied to the back channel.	37
Figure 14. Turn-on voltage for devices with varying channel thickness with and without ODPA passivation. 95% confidence intervals are also shown.	39
Figure 15. TFT hysteresis between V_G up and down sweeps for devices with and without ODPA on the IGZO channel surface.	40
Figure 16. Subthreshold swing for various thicknesses of IGZO channels with and without ODPA. The vertical bars indicate 95% confidence intervals.	41
Figure 17. Average mobility of IGZO TFTs with different channel thicknesses, with and without ODPA. The bars shown 95% confidence level.	44
Figure 18. Band diagrams of IGZO channel in the bulk and at the dielectric and back channel interface. a) shows band diagram with bare IGZO exposed air. b) Shows the band diagram with ODPA bidentatly bonded to the IGZO surface.....	46
Figure 19. I_{on}/I_{off} ratio for different IGZO channel thicknesses with and without ODPA on the back channel. The bars shown 95% confidence level.....	47
Figure 20. Schematic diagram of a LCD pixel. Transmission of polarized light from the back panel is controlled by rotation of liquid crystals. TFTs provide control over the rotation of liquid crystals. “Reprinted from NPG Asia Mat.1 / 1, Kim K.H., Song J.K., Technical evolution of liquid crystal displays, 29-36, Copyright (2009), with permission from Nature Publishing Group.”.....	50
Figure 21. Pixel and subpixel array for the Samsung Galaxy S4 Mini.....	51
Figure 22. Different droplet ejection modes generated by varying the voltage pulse amplitude. Note the droplet size difference between droplet and nozzle diameter. “Reprinted from J. Aero. Sci., 46, M.W. Lee et al., A study of ejection modes for pulsed-DC electrohydrodynamic inkjet printing, 1-6, Copyright (2012), with permission from Elsevier.”.....	53
Figure 23. Forces induced on a fluid in the presence of an electric field at the tip of a needle.	56
Figure 24 Optical image of IGZO substrate with printed a) SU-8 and b) HPA lines with a line width of 4 and 2 μm , respectively.....	62

LIST OF FIGURES (Continued)

<u>Figure</u>	<u>Page</u>
Figure 25. Optical microscope images of EHDP IGZO patterning process. a) SU8 printed on IGZO pad. b) SU8 and IGZO post etch. c) SU8 removed with only IGZO channel remaining. Channel width in these images is $\sim 25\mu\text{m}$ and length $\sim 750\mu\text{m}$	64
Figure 26. Microscope images of printed lines on IGZO using a) HPA and b) SU-8. Final devices with etched IGZO and Al source and drain patterned using c) HPA and d) SU-8. c) The width of the HPA patterned channel is $\sim 2\mu\text{m}$. d) the width of the SU8 patterned channel is $\sim 4\mu\text{m}$	65
Figure 27. Schematic of EHDP patterned IGZO TFT. Probes for the source, drain, and gate were connected at V_s , V_D , and V_G respectively.	66
Figure 28. Changes in printed HPA line width as pulse frequency is varied. Line widths shown are 17, 17, 22, and $28\mu\text{m}$ for 200, 100, 60, and 40 Hz, respectively. Bias = 350 V, pulse height = 100, pressure = 0.5 psig, needle diameter = $5\mu\text{m}$. Stage velocity was held constant at $0.12\mu\text{m/s}$	68
Figure 29. Optical microscope image of $4\mu\text{m}$ wide lines printed with SU8 on IGZO surface.	72
Figure 30. a) HPA patterned IGZO TFT with channel width $\sim 2\mu\text{m}$. b) SU8 patterned IGZO TFT. Source and drain is Al and the gate dielectric is SiO_2 . IGZO channels are $100\mu\text{m}$ long and 50nm thick.	73
Figure 31. a) I-V transfer characteristic current output for IGZO TFTs patterned using HPA, normalized using L/W. b) Average mobility of HPA patterned TFTs. The arrows indicate the direction of the sweep.....	74
Figure 32. a) I-V transfer characteristics of IGZO TFT patterned using SU8, normalized using L/W. b) Average mobility of SU8 patterned TFTs. The arrows indicate the direction of the sweep.	75

LIST OF TABLES

<u>Table</u>	<u>Page</u>
Table 1. Trap state density of IGZO with and without ODPA, calculated from the SS using Equation 7.	43
Table 2. Printed line widths using various needle diameters.....	67
Table 3. EHDP printing parameters for producing 2 um features using HPA ink.	69
Table 4. EHDP printing parameters for producing 4 um features using 0.15% (wt) SU8 in cyclopentanone.	71
Table 5. Summary of TFT electrical parameters for IGZO channels patterned using EHDP and unpatterned	76

Chapter 1: Introduction

Next Generation Electronics

Consumer demand for faster, energy efficient, more durable, portable electronics pushes the need for developing new materials and processes for next generation applications. Sensors are a crucial component for human interactions with electronics, where electrochemical sensing of molecules or mechanical sensors has led to vast improvements in quality of life for consumers. Patients with Type-I diabetes can tightly control their glycemic levels using continuous monitoring and delivery systems that control insulin levels in real time [1], [2]. For these systems to be of practical use, the patient needs to retain their mobility while using the system. Size reduction in sensors allows for the development of portable glucose sensing and delivery systems. These electrochemical sensors should be small enough to be minimally invasive while implanted in the body. Other chemical sensors such as gas and DNA greatly benefit from miniaturization by allowing the sampling and analysis to be done on site wherever the test is required [3], [4]. Portable products such as smart phones require increased processing speeds to meet the versatile computing needs of users. Increasing the capabilities of portable personal computing devices such as smart phones comes with a drawback by requiring higher power consumption in devices limited by battery storage capacity. New materials that draw lower power but have electrical performances equal or greater to their predecessor are needed to meet the increased computing needs while retaining portability.

Among other consumer technologies that are greatly desired are transparent displays and flexible displays. Transparent displays are a technology that has wide spread applications [5]. For example, vehicle windows equipped with transparent displays can indicate crucial information to the driver without obstructing their view to the outside world. To obtain fully transparent displays, all the materials used must be transparent within the visible spectrum. This requires conducting and semiconducting materials with wide band gaps. Specialized polymers and amorphous oxides have shown to be possible candidates [5], [6].

Amorphous oxides have also shown applications in flexible electronics [7]–[9]. Bending of a film causes tangential stresses along the plane normal to the surface. Flexible electronics require the components to retain their electrical properties while exposed to bend induced stressing [10], [11]. Mechanical failures such as cracking or delamination occur from excessive stresses and these failures degrade the electronic properties of components in the device [12]. Amorphous oxides have been shown to have higher resistances to failure when subjected to bending stresses [11]. Indium-gallium-zinc-oxide (IGZO) has shown potential as a semiconducting material for sensing, transparent, and flexible displays [4], [7].

Thin Film Transistors

Transistors are a crucial component for most electronic devices. They act as the physical components in logic gates required for digital circuits or as switches for displays. A

typical bottom gate thin film transistor is shown in Figure 1. The channel is composed of a semiconducting material. Conducting materials such as metals, conductive polymers, or conductive oxides are used for the source, drain, and gate.

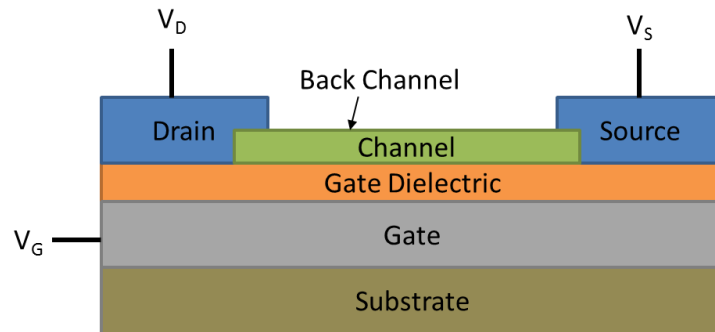


Figure 1. Typical bottom gate structure TFT.

When a constant bias is kept between the source (V_S) and drain (V_D) a current flows through the channel from the source to the drain, when the device is at its on state. The threshold voltage (V_{th}) is the gate voltage required to create a conducting pathway through the channel [13]. The channel's conductance can be controlled by changing the carrier concentrations in the conduction band [13], by applying a gate voltage (V_G) low amounts of current flows through the channel when the device is off ($V_G < V_{th}$). A significant increase in current flows through the channel when the device is on ($V_G > V_{th}$). The gate dielectric blocks the flow of electrons from the gate to the source or drain. The dielectric allows an increase in the electric field imposed by V_G to influence the channel conductivity [13]. The back channel is the interface located across from the channel/gate dielectric interface. These components all work together to modulate channel conductivity allowing for switching between on and off states, as is required for switching pixels in displays.

The relative number of donors and acceptors in a semiconductor indicates if it is an n-type or p-type semiconductor [13]. All semiconductors contain acceptor and donor charge states above 0 K. Donor states are negatively charged and contribute an electron to the conduction band. Acceptor states are electron deficient and contain positively charged holes that can be excited into the valence band. N-type semiconductors have a majority of negatively charged electron carriers, and p-type semiconductors contain a majority of positively charged hole carriers [14]. Since IGZO acts as an n-type semiconductor only n-type devices will be discussed from this point on.

Thin film transistors (TFT) are a common class of transistors. TFTs differ from traditional metal oxide semiconductor field effect transistors (MOSFET) mainly by their fabrication methods [15]. TFTs are fabricated by serial deposition and patterning of thin films of functional materials to form a transistor. The deposited films intrinsically exhibit their desired electrical properties with little or minor post deposition processing requirements. Traditional MOSFET fabrication generally involves modifications to a monolithic substrate, typically crystalline silicon, to alter electrical properties [16]. The films in MOSFETs must undergo many processes to reach the required electrical properties. Ion doping and diffusion processes require complex, high energy, and high temperature processes to achieve the desired electrical properties [16].

While TFTs may not always offer the flexibility or the highest performance compared to MOSFETs, they do offer advantages in relatively simpler processes, such as plasma

sputtering, and potentially easier post process requirements, and applications to large areas [15]. Amorphous films can be deposited using sputtering allowing for deposition of amorphous oxide semiconductors [14]. Plasma sputtering has been successfully implemented for large area manufacturing of electronic displays [13]. Polymer substrates are also compatible with sputtering due to the low deposition temperatures that can be achieved. The mechanical properties of polymer substrates make them ideal for use in flexible displays.

TFTs can be used for both chemical and mechanical sensing [4], [17]–[19]. One type of electrochemical sensor measures current generated by the oxidation and reduction of the analyte [20]. The sensitivity of these sensors depends on the sensor's ability to measure current or modulate the gate potential generated from the reaction. The size and electrical properties of TFTs allow them to be highly sensitive to their environment. These sensitivities can be utilized for sensing by measuring changes in the TFT response such as threshold voltage or conductance [18], [21], [22]. The back channel can be functionalized using SAMs to promote chemical reactions with the analyte of interest [22]. The reactions cause local changes in electric properties that change the TFT's response. The high sensitivity allows for molecular detection at lower concentrations. The small size of TFTs allows for dense packing of multiple sensors on a single chip. The cost of these chips can be reduced by using industrial mass production processes currently available.

Thin Film Transistor Electrical Properties and Characteristics

The threshold voltage (V_{th}) is defined as the minimum gate voltage required to generate a conductive pathway within the channel [13]. For AOSs the value of V_{th} is dependent on the number of carriers in the channel [23]–[25]. V_{th} near 0 V is often desirable for obtaining devices with lower power consumption. The field effect mobility (μ_{FE}) relates carrier velocity in an electric field [13]. This velocity is a ratio of free carriers to trapped carriers [26]. The highest possible mobility is usually desired as higher carrier mobilities enable higher currents to pass through smaller devices. The subthreshold swing (SS) measured in V/decade relates the current output to the gate potential [13]. Low SS means that lower ΔV_G , when $V_G > V_{th}$, is required to increase the output current to turn on the device. The value of SS is governed by the sub-bandgap trap state densities in the channel [27]. The I_{on}/I_{off} ratio is the ratio of current in the on state to the current in the off state. Low off state currents are important for reducing noise and leakage while the device is turned off. The on state current can be defined as a specific current when the device is turned on. The channel current, threshold voltage, mobility, subthreshold swing, and on/off ratio are all dependent on device geometry [13]. The output current is normalized using the channel length and width. Normalization allows for devices with different channel lengths and widths to be directly compared with each other. Methods used to measure TFT performance and calculate these parameters are discussed in Chapter 2. More in-depth discussion of these electrical parameters is presented in Chapter 3.

The electrical properties of amorphous oxide semiconductor (AOS) TFTs are highly sensitive to their environment. These sensitivities can be used for chemical sensing of the TFT's local environment [19], [21], [22]. Local chemical changes from molecules absorbed to the back channel can change the V_{th} , mobility, SS and on/off ratio. TFTs can be used as a sensor by understanding how molecules exposed to the IGZO back channel changes the channel properties. The high sensitivity of these parameters amplifies the sensors sensitivity.

Indium Gallium Zinc Oxide

The semiconducting material examined in this thesis is indium gallium zinc oxide (IGZO). IGZO is currently used in a range of LG and Sharp electronic displays [28], [29]. IGZO TFTs operate as n-type semiconductors due to their high donor concentrations [30]. IGZO is transparent to the visible spectrum with a band gap of ~ 3.1 eV. The amorphous state of IGZO means no grain boundaries form, where grain boundaries can cause variations in electrical properties. IGZO can be uniformly deposited over large areas using plasma sputtering making it an excellent option for large area display manufacturing [31], [32]. As deposited IGZO can readily obtain exceptional field effect mobilities > 3 cm²/V s, while laser or thermal annealing below the crystallization temperature further increases the mobility to above 10-40 cm²/V s [33], [34]. An interesting characteristic observed in IGZO and other AOSs is that V_{th} shifts positive as channel thickness is decreased [24], [35], [36]. For AOSs, the location of V_{th} is dependent on the absolute number of carriers. As the channel thickness is decreased the number of

free carriers is decreased causing ΔV_{th} to shift positively. The value of V_{th} can also be controlled by thermal annealing and varying oxygen concentrations during deposition [37]. As the thickness is decreased surface states become more important, influencing device operation. Absorbed oxygen and water act as electron acceptors and donors, respectively, for the IGZO channel [38]. Atmospheric water and oxygen absorbed to the TFT back channel can vary the electron carriers causing instabilities in V_{th} [39].

Passivation of the IGZO back channel using insulators such as TiO_2 , SiO_2 , Al_2O_3 and photoresist has been shown to increase stability ΔV_{th} by blocking absorption of atmospheric contaminants to the back channel [40], [41]. For sensors the IGZO channel needs to be exposed to the environment. The use of self-assembled monolayers can act as a protective coating while allowing the channel to be influenced by the environment.

Self-Assembled Monolayers

Self-assembled monolayers (SAM) are molecules that readily form a single molecular layer on a material. The SAM consists of a head and tail group. The head group chemically reacts with the substrate and binds the SAM to the surface [42]. The tail group does not bind to the surface and is used to modify the surface properties of the underlying surface. Because the head group only binds to the surface a self-limiting mono layer of molecules is formed on the surface. Thiol head groups have been observed to spontaneously adsorb to noble metals such as gold [43]. Silanes and phosphonic acid head groups adsorb to oxide surfaces [44], [45]. An example of a phosphonic acid with tail group "R" bound to an oxide surface is shown in Figure 2. The tail group can be

chosen to tailor the surface properties. For instance surfaces can be modified to become hydrophobic or hydrophilic depending on the tail group used.

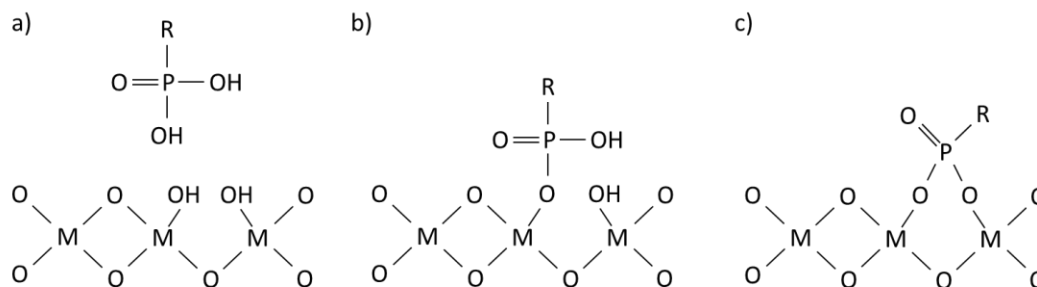


Figure 2. a) Phosphonic acid SAM and example oxide surface. b) SAM bound to surface as monodentate. c) SAM bound as tridentate. The R group can be chosen to provide the desired surface properties.

In Chapter 4, n-hexyl phosphonic acid (HPA) is used to create hydrophobic regions on IGZO surfaces for selectively etching structures using aqueous HCl as an etchant. The HPA is used for patterning IGZO channels for TFTs.

SAMs can be used for passivating exposed back channels on IGZO TFTs to improve stability. Oxygen and water absorbed to the back channel surface of IGZO and other AOSs can affect TFT performance by altering the carrier concentrations. Densely packed SAMs can form a barrier layer to prevent molecules from absorbing to the bare IGZO [46]. Different tail groups can cause band bending at the back channel [47]. The effects of band bending on the surface becomes more pronounced as the channel thickness is reduced. Alternatively SAMs can be used to modify TFT back channels for molecular detection [22]. The tail group of SAMs can be tailored to selectively interact with

molecular analytes. The chemical interactions produce local changes in the IGZO energy bands. The changes in band energies and carrier concentrations reproducibly alter TFT behavior. A range of analyte concentrations can be quantified by calibrating TFT electrical responses to various known concentrations of analyte. High sensitivity and wide detection ranges have been demonstrated in glucose TFT sensors functionalized using SAMs [22]. As the thickness of the channel is reduced, the IGZO back channel surface becomes more apparent in the TFT electrical response. Understanding how SAMs can influence IGZO TFT behavior as the channel is reduced is important to developing smaller TFT chemical sensors. Chapter 3 examines the application of octadecylphosphonic acid (ODPA) and HPA on the back channels of IGZO TFTs with various channel thicknesses.

Fabrication of Thin Film Transistors

TFTs are fabricated using a variety of methods. Films can be deposited using sputtering, chemical vapor deposition, pulsed laser deposition, electrodeposition, solution based condensation reactions [14], [16]. Most of these methods, except electrodeposition, cover the entire substrate with a homogeneous film and need to be further patterned to obtain the desired structures. Photolithography and etching is commonly used for patterning of TFT and other electronic structures. The process of photolithography using a negative tone resist is outlined in

Figure 3.

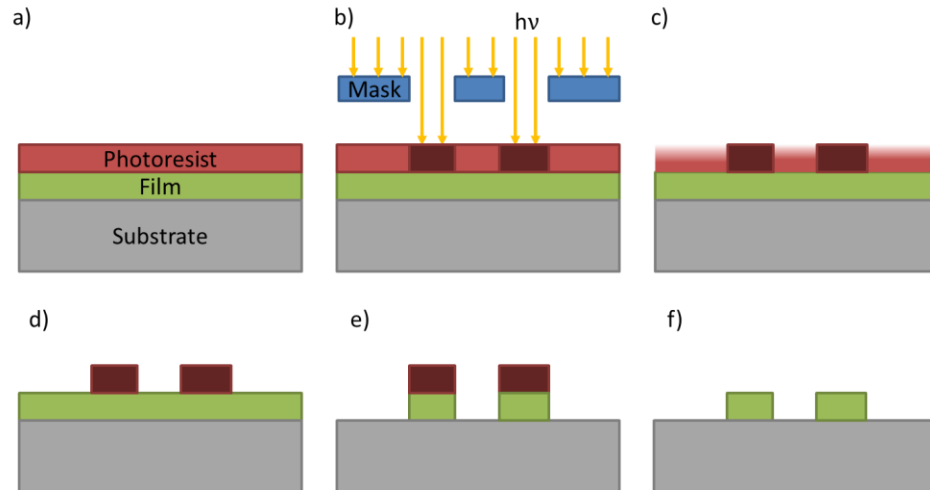


Figure 3 a) Photoresist spin coated onto substrate. b) Selective radiation exposure using mask. c) Solubility change in photoresist, soluble regions removed using developer. d) pattern to be transferred by photoresist etch remains. e) Exposed regions are etched. f) Photoresist stripped leaving desired pattern in thin film.

This process requires first coating the blanket films with a photoresist as shown in Figure 3a. The photoresist is designed to change solubility when exposed to radiation. A mask is positioned over the resist to isolate regions from radiation as shown in Figure 3b. The development step shown in Figure 3d, uses a chemical developer to remove the soluble regions. The exposed regions of the underlying film is then etched using solution based etchants or plasma etching shown in Figure 3e. Finally the remaining photoresist is stripped from the substrate leaving only the patterned thin film shown in Figure 3f. Photoresist can be deposited and patterned prior to the thin film deposition to selectively deposit films without etching using a lift off process. Complex electronic structures are built by repeating these deposition and patterning steps.

Drop on demand printing, or digital patterning, of solution based functional materials is another method for selectively patterning thin films. Printing allows for direct patterning of materials without the need for photolithography. The process of digital patterning is shown in Figure 4.

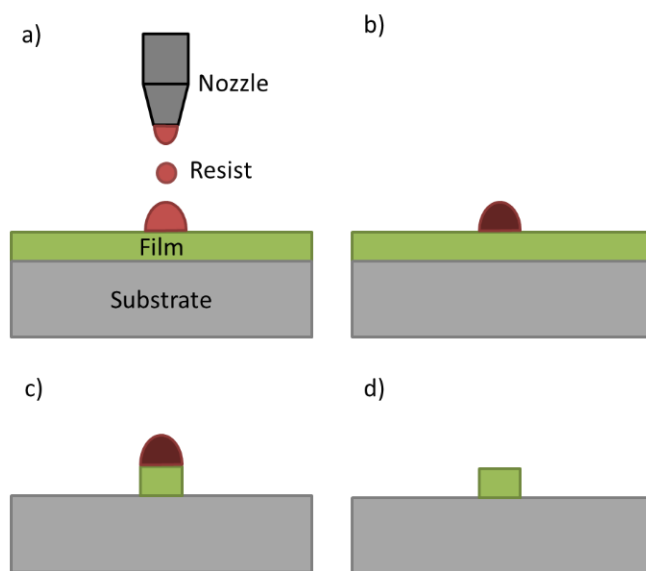


Figure 4. Digital patterning of a thin film. a) The resist is selectively patterned on the film. b) For photoresist, heat is applied to crosslink and harden the resist. c) Etching solution is used to remove the exposed film. d) The resist is removed leaving the desired pattern.

In Figure 4a, the resist is printed in the desired pattern. Figure 4b shows the resist forming a protective layer above the underlying film, where heat is applied to promote crosslinking in the photoresist. Figure 4c the film is etched. Figure 4d the resist is removed leaving the underlying film with the desired pattern. Printing can be advantageous due to reduced material consumption and does not need energy intensive vacuum and radiation systems. The high speed and selective deposition capabilities of printing make it suited for industrial mass production. However, solution deposition of

electronic materials requires specialized solution based chemistries, and it can be difficult to achieve film qualities with qualities that match vacuum deposited films. Adapting existing solution based processes to printing methods may provide easier routes for reducing total production costs. Solution based photoresist, such as SU8, can be modified for printing as an etch resist without the requirement of radiation exposure. Self-assembled monolayers can also be printed to modify the thin film surface and act as an etch resist. The 4th chapter of this thesis focuses on electrohydrodynamic ink jet printing of SU8 and HPA as an etch resists for fabrication of TFTs.

Electrohydrodynamic Ink Jet Printing

Reducing the size of TFTs and other electrical components is crucial to increasing circuit density. One of the major draw backs to conventional printing of functional materials for fabricating TFTs is the printing resolution limits often encountered. Piezoelectric and thermal ink jet printers are the most common systems used for drop on demand printing. These systems rely on generating pressure forces to eject droplets from the print nozzle. The formation of droplet size is limited by the generated pressure wave, fluid's surface tension, and viscosity. The practical resolution to these systems is 10-30 μm [48].

Electrohydrodynamic ink jet printing (EHDP) is a printing method in which an electric field is used to generate droplets. The electric field concentrates ions and deforms the meniscus into a cone shape, known as a Taylor cone [49]. When the repulsive ionic forces overcome the surface tension forces a droplet is ejected. The ejected droplet is

generated only at the tip of the Taylor cone which provides droplets with diameters smaller than the nozzle diameter. This droplet generation technique can easily achieve resolutions sub 10 μm [50]–[52]. Here EHDP is used to demonstrate printed etch resists for patterning TFT channels with narrow channel widths ($<5 \mu\text{m}$). The smaller printed feature sizes offered by EHDP can be used to realize even smaller printed circuits. Successful printing of SAMs demonstrates that EHDP can be used to deposit SAMs for modifying and functionalizing IGZO channels. Further details of printing and EHDP will be described in Chapter 4. The development of EHDP can help achieve cheaper manufacturing of smaller integrated circuits and sensors.

Chapter 2: Instruments and Techniques

Semiconductor Parameter Measurements

Electrical measurements for TFTs are made using a semiconductor parameter analyzer (Agilent 4155C) and probe station (Alessi REL 4800). The probe station provides structural support, and positioning of the probe needles with respect to the sample stage. The housing of the probe station is closed to provide a dark environment to prevent light induced current and instabilities. Needle like tungsten probes, held using micromanipulators, are used to make contact with the TFT electrodes. A microscope on the probe station is used to ensure good contact between the electrodes. The positioning of the probes on the TFT source, drain, and gate electrodes is shown in Figure 5.

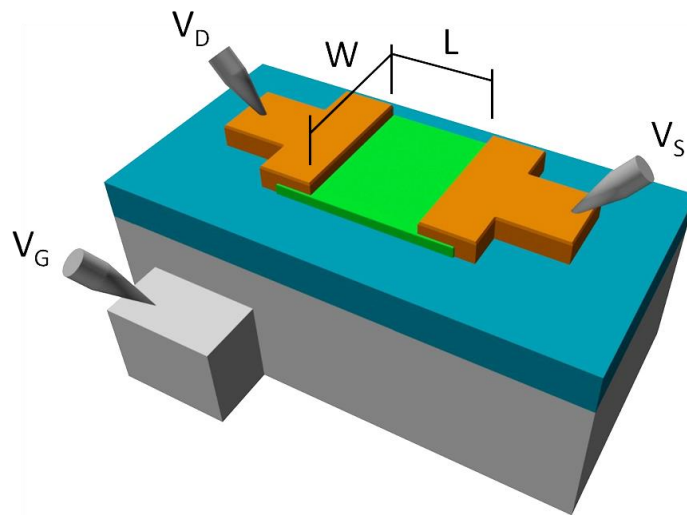


Figure 5. Semiconductor parameter analyzer probe placement on source, drain, and gate electrodes for a TFT. L is the channel length from source to drain. W is the channel width.

The semiconductor parameter analyzer (SPA) individually controls the voltage while measuring the current for each probe. The Agilent 4155C SPA can measure currents from the pico to milliamp range [53].

TFT current-voltage (I-V) transfer characteristic curves are generated by setting the drain voltage (V_D) and sweeping the gate voltage (V_G), while measuring current at all three electrodes. The output drain (I_D) current, at V_D , for a single sweep is plotted various ways to obtain different parameters. A typical I-V transfer plot is shown in Figure 6, for an n-type TFT, with $\log I_D$ of current plotted on the left axis and I_D on the right axis. For the measurements performed here, V_G is swept from negative to positive and back down to the starting value. When sweeping V_G from low to high and back from high to low there can be a shift in the V_G for a given current, which is called hysteresis. This hysteresis can be caused from instabilities caused by trapped charge in the channel or gate dielectric [54].

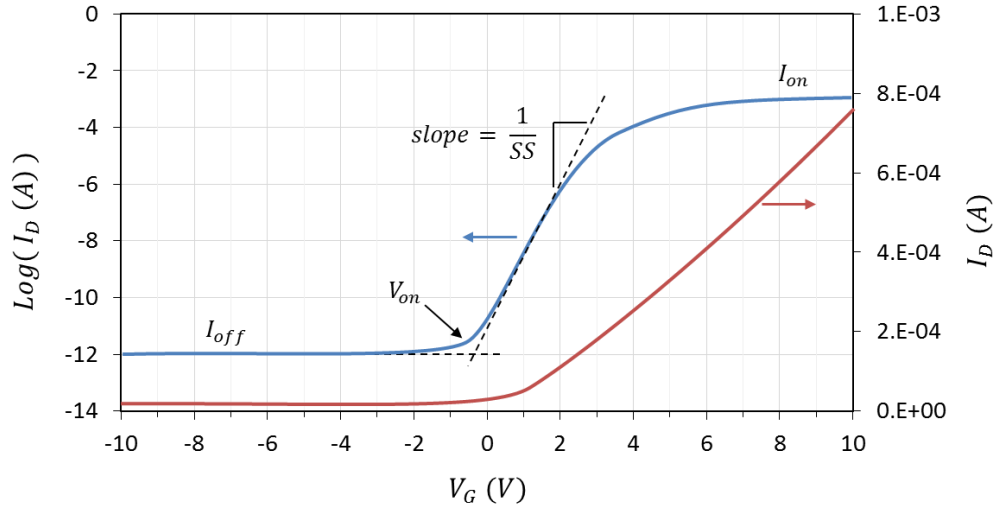


Figure 6. Typical TFT I-V transfer plot for n-type AOS TFT. The gate voltage is swept and the $\log I_D$ of output current is plotted on the right for identifying mobility and subthreshold swing. Square root of I_D is plotted on the right for identification of turn-on voltage.

Plotting the output current on the two different axes helps to graphically obtain important TFT parameters. The current through the device is strongly related to the device geometry. In order to retrieve intrinsic properties and compare devices with different geometries, the current is normalized using the device geometry where L is channel length from source to drain, W is the channel width. When $V_D \gg V_{th}$ the channel operates in saturation mode, where the channel induced current reaches a maximum, and I_D is independent of V_G [55]. This behavior is due to the high drain voltage fully depleting the carriers at the drain, and the current is limited by the depleted drain region [56]. However, when $V_D < V_{th}$ the device operates in linear mode, where I_D increases linearly as V_D increases. In linear mode, carriers still exist at the drain and can be excited into the conduction band by V_G . The drain output current in TFTs can be approximated using the gradual channel approximation for operating in linear mode, given in Equation

1 [56]. C_g is the gate dielectric capacitance, μ is the mobility, W is the channel width, and L is the channel length. The turn-on voltage (V_{on}) is used instead of V_{th} for determining I_D . V_{on} is defined as the point at which current begins to rise when plotted $\log(I_D)$ vs V_G , as shown in Figure 6. V_{on} and V_{th} are different, but share similarities and are affected similarly by channel properties such as carrier and defect concentrations. The devices examined in this thesis were operated in linear mode and V_{on} is used for IGZO TFT characterization.

$$I_D = \frac{W}{L} \mu C_g V_D \left(V_G - V_{on} - \frac{V_D}{2} \right) \quad (1)$$

In linear mode, carrier transport is sensitive to both bulk and interface defects; interface effects become more significant. V_{th} is used in context of an ideal MOSFET, but is insufficient for determining current through the non-ideal semiconductors such as IGZO while operating in linear mode; V_{on} is better used for modeling AOS TFTs behavior operating in linear mode [57].

The average mobility (μ_{avg}) is non-linear and is a function of V_G . The average mobility can be evaluated from the experimental I-V transfer curves, using Equation 2 [55]. Where g_m is the transconductance ($\Delta \log(I_D) / \Delta V_D$).

$$\mu_{avg} = \frac{L g_m}{W C_g (V_G - V_{on})} \quad (2)$$

The inverse of the subthreshold swing is calculated by finding the maximum slope of the log normalized output current shown in Figure 6. Current through the channel is primarily due to charge transport through the semiconductor between the biased drain and the source. The off current (I_{off}) is the current that is observed while $V_G < V_{\text{on}}$. Gate leakage can be measured as a current through the gate dielectric and is monitored by measuring current between the gate and source electrode. The on current (I_{on}) can be defined as the output current required by device specifications. For these experiments the highest current achieved is used as the on current. The $I_{\text{on}}/I_{\text{off}}$ ratio is calculated by the ratio of on current to off current.

The turn-on voltage, mobility, $I_{\text{on}}/I_{\text{off}}$ ratio, and subthreshold swing are important parameters for examining device physics and TFT computer modeling. More on the details of these parameters and their significance will be presented in Chapter 3.

Electrohydrodynamic Ink Jet Printer

A custom built electrohydrodynamic ink jet printer was used to print etch resist which is used to pattern the channel width on the micron scale. A schematic of the printing system is shown Figure 7. Glass pre-pulled needles (World Precision Industries), with inner diameters of 1 and 5 μm , were sputter coated with $\sim 20\text{nm}$ of Au/Pd (40/60) to provide high conductivity. A high voltage amplifier (Trek 677B) is used to apply a voltage to the metal coated needle with the substrate held at ground. The self-assembled monolayer, 1H,1H,2H,2H-perfluorodecanethiol (Sigma Aldrich), was used to modify the Au/Pd

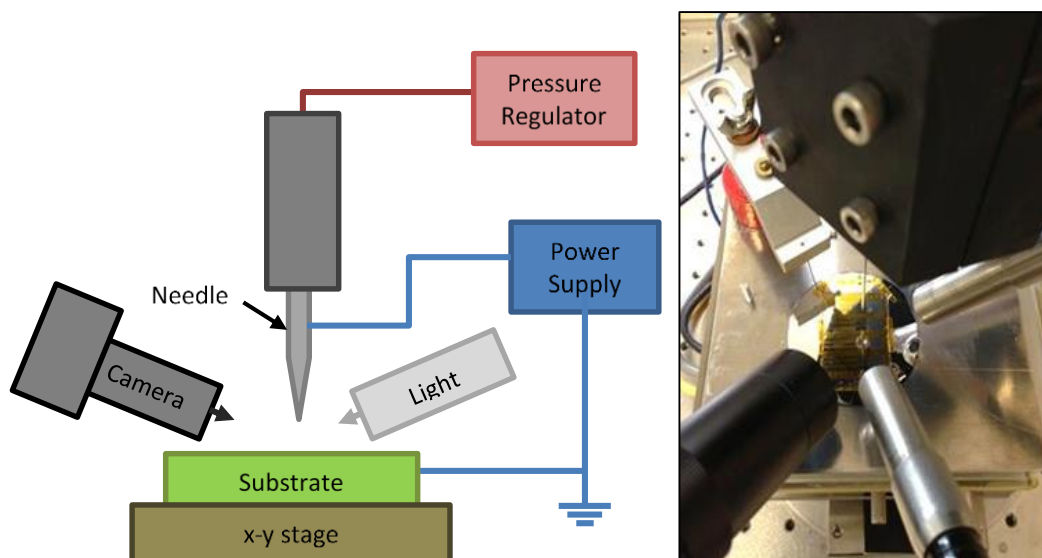


Figure 7. a) Schematic diagram of EHD printing system. b) Image of printing stage, light sources, ground needle, and printing needle.

surface by dipping the needle in 5 mM SAM in ethanol for 5 minutes. This surface treatment provides a hydrophobic surface that reduces hydrophilic ink wetting of the outer surface of the needle.

The position of the stage and substrate can be translated using linear x and y axis stepper motors (Parker MX80L TO3MP). Video feedback is provided using a microscope camera (Edmund Optics Infinity2). The needle tip was held at a constant height above the substrate with a constant air pressure applied to the back of the needle. The height of the needle is controlled by a z-axis stepper motor (Parker MX80ST 02MSJ). Back pressure is controlled using pressure transducer (ControlAir 500-AF). The pressure helps deliver ink from the syringe barrel to the tip of the needle. All hardware is controlled using custom LabVIEW software.

Printing is achieved by biasing the needle with respect to the grounded substrate. The bias results in the formation of a Taylor cone, and a square voltage pulse is used to control droplet generation timing and placement. The droplets generated from the square pulse is shown in Figure 8.

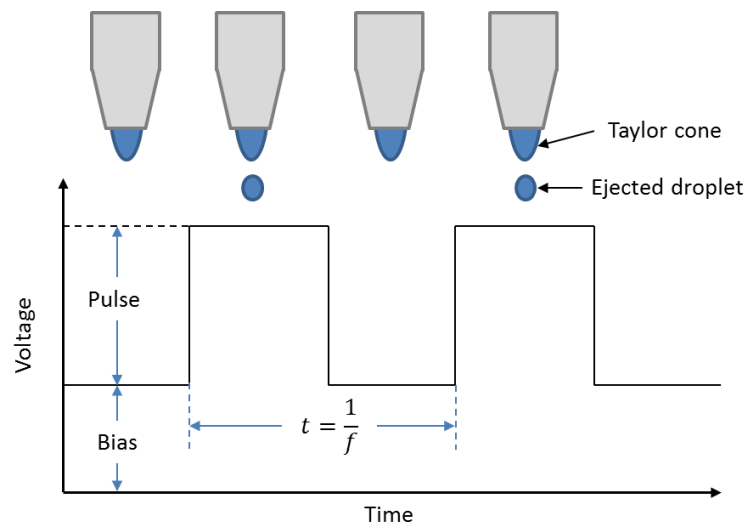


Figure 8. Voltage bias between the needle and substrate with a square pulse applied at a constant frequency. The bias maintains the Taylor cone at the tip and each pulse ejects a single ink droplet.

Where the time between pulses (t) is controlled by the frequency (f). Careful control of the pressure, height, potential bias, pulse height, and pulse frequency can be used to print small droplets onto the substrate. The details of optimizing these parameters for specific inks will be discussed in Chapter 4.

Chapter 3: Self Assembled Monolayers Applied to the Back Channel of IGZO Thin Film Transistors

Introduction

Next generation digital displays require new materials to meet consumer demands.

Demands include enhanced product lifetimes, durability, higher resolution, and reduced power consumption [58]. By their nature, portable electronics require low energy consumption and excellent durability. Flexible displays are another desired technology requiring new semiconducting materials that can retain their electrical properties when stressed by applying curvature [7]. Polymer substrates are favored for flexible technology due to their ability to withstand large radii of curvature [59]. The use of polymeric substrates requires low temperature processing ($<300\text{ }^{\circ}\text{C}$) to limit damage to the substrate which makes traditional silicon processing techniques incompatible. Furthermore, flat panel displays require materials that can be uniformly deposited over large areas, and product lifetimes (10,000 hours) necessitate the need for stable devices with prolonged use and storage.

Molecular sensors with lower detection limits and larger detection ranges can be realized using TFTs as the sensing component [19]. The inherently small size of TFTs allows for array of sensors on a single chip. These arrays can include redundant sensors for increased accuracy or multiple sensors for sensing different molecules. Functionalizing the back channel of TFTs with molecules that react with the analyte of interest can lead to

electrical changes that can be used for molecular detection. Functionalization can be accomplished by using SAMs or reactive thin film membranes such as enzymes [3], [22].

Amorphous oxide semiconductors (AOS) show good promise for use in many next generation electronics [60]. In particular, amorphous indium gallium zinc oxide (IGZO), meets many of these processing and electrical requirements electronics [61]. IGZO TFT sensors capable of detecting glucose, pH, and gases such as ammonia and NO have been demonstrated [22], [62], [63]. A full understanding of IGZO must be realized in order for its integration into consumer products. Knowledge of instabilities is crucial for developing durable products with prolonged lifetimes. Instabilities in IGZO TFTs are attributed to charge trapping in the gate dielectric, in the bulk channel, at the channel/insulator interface, at the back channel surface, and deep acceptor traps [24]. As the thickness of the IGZO channel decreases, surface states at the exposed back face become more prominent in the TFT performance [36], [64]. The reduction in surface states and absorbed species improves stability and hysteresis of the threshold voltage. It is believed that absorbed oxygen acts as an electron acceptor and water acts as an electron donor [65], [66]. The absorbed species alter the concentration of carriers and causes changes in V_{th} . For example, increases in carrier concentration decreases both V_{th} and V_{on} . The existence of surface states results in instabilities in TFTs which limits their application in displays. Self-assembled mono layers (SAM) can be used to passivate the back channel and reduce surface trap states. SAMs are molecules composed of a head, spacer, and tail group. The head group reacts with the oxide to covalently bond to the

surface and the tail group prevents further layers from attaching, creating a self-limiting monolayer. In this thesis the TFT performance with different IGZO thicknesses was compared with and without the application of SAMs to the back channel. The use of SAMs on the back channel of TFTs improves the electrical stability of TFTs and provides means to examine the effects of the exposed back channel chemistry on performance. Understanding how SAMs modify the back channel chemistry can also help to further develop functionalized IGZO surfaces for molecular detection.

Amorphous Oxide Materials and Processing Requirements

AOSs must have enhanced properties for thin film in order for to replace Si TFT technologies for these applications. IGZO meets many of the processing and electrical requirements for next generation electronics [60]. Examples of other AOSs are zinc tin oxide (ZTO)[55], hafnium indium zinc oxide (HfIZO) and indium zinc oxide (IZO) [64], [67]. Amorphous silicon (a-Si) is an industry standard for displays but suffers from poor mobility ($> 1 \text{ V/cm}^2 \text{ s}$) and stress induced hysteresis [68]. Amorphous materials do not contain grain boundaries that are known to cause short range variations in electrical properties in polycrystalline materials, i.e. polysilicon (p-Si) devices [69]. The use of polymers in flexible displays poses another challenge for manufacturing. Processing temperatures for polymer substrates must be kept below the glass transition temperature, typically 100-300 °C depending on the polymer [70]. Thin film semiconductors must be deposited uniformly over large areas for use in large screen consumer displays. Non-uniformities cause variations in electrical properties which limit pixel brightness

uniformity across the display and decrease device reliability. Low temperature deposition methods such as pulsed laser deposition and sputtering can be used to deposit IGZO [71]–[73]. TFTs using IGZO channels can have mobilities ranging from 4–40 V/cm² s [71], [72], [74]. Low temperature post deposition annealing (>400 °C) has been shown to further enhance mobility [75]. IGZO is transparent in the visible spectrum making it excellent for use in traditional and fully transparent displays. Full color 12.2” WXGA AMOLED, 15” XGA AMLCD, and 32” AMLCD displays, along with a 2.4” fully transparent display have been demonstrated using IGZO TFTs [31], [32], [60]. Flexible displays have also been fabricated using IGZO TFTs [7]. Currently LG, Samsung, and Sharp are producing 32”–50” displays for the consumer market [28], [29]. Apple uses these display manufactures IGZO displays for their next-generation high resolution Retina display [76].

IGZO Structure & Electron Transport

The structure of amorphous IGZO is complicated due to its highly disordered nature. IGZO deposited by pulsed laser deposition or sputtering remains amorphous until 500 °C [77]. X-ray diffraction (XRD) measurements on IGZO films annealed (400–600 °C) is shown in Figure 9a. where amorphous halo peaks at 34° and 58° for samples annealed up to 500 °C are observed [77]. Sharp peaks emerging after annealing to temperatures above 500 °C, and are attributed to crystallization of IGZO. Post deposition annealing of IGZO films can drastically alter device performance. Figure 9b. shows that the Hall mobility of “low quality” amorphous IGZO increases with annealing temperature, where the mobility

saturates just before the onset of crystallization [77]. The increase in mobility is attributed to structural relaxation and reduction of trap states. It should be noted that while the mobility of crystalline IGZO is the highest, it requires a higher processing temperature. One of the major advantages of AOSs is that their low thermal budget is compatible with low temperature processes and polymer substrates.

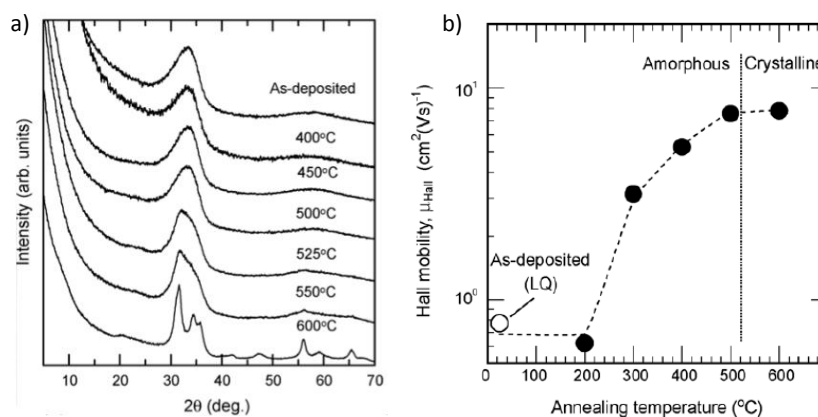


Figure 9. a) XRD patterns of deposited amorphous IGZO annealed 400-600 °C. Onset of crystallization is observed at 525 °C. b) Mobility of deposited amorphous IGZO annealed 0-600 °C. “Reprinted from *Phys. Stat. Sol.*, 205 / 8, Nomura *et al.*, Relationship between non-localized tail states and carrier transport in amorphous oxide semiconductor, In-Ga-Zn-O, pg. 1910-1914 Copyright (2008), with permission from John Wiley and Sons.”

The conduction band minimum (CBM) in IGZO is composed of unoccupied s orbitals located on the heavy metal cations [26], while the valence band maximum (VBM) is primarily composed of the oxygen 2p orbitals. The large non-directional overlapping of s orbitals is what allows amorphous IGZO and other AOSs to have large electron mobilities. In contrast the low mobility in a-Si results from the directionality of sp^3 their poor overlap for disordered materials [78]. The temperature dependent mobility can be explained using Alder’s percolation theory, where carriers can follow multiple

conduction pathways [78]. At low temperatures the carriers take longer paths related to the lowest energy pathways. At higher temperatures the carriers can be thermally excited into higher energy levels allowing them hop over higher energy barriers and take a more direct path.

TFT Mobility

The carrier mobility is a parameter used to describe the conductivity of charge carriers in an electric field [13]. It is an important parameter for TFT performance as it is required to describe and model the on-state current through a semiconductor channel. In AOSs the mobility is dictated by the total free carrier density (N_{GS}) in the film and the number of density carriers trapped by defects ($N_{t,tot}$) [79]. The equation for field effect mobility (μ_{FE}) relating the carriers and carrier traps is shown in Equation 3 where μ_d is the drift mobility. The difference in N_{GS} and $N_{t,tot}$ represents the number density of untrapped carriers moving from source to drain. The measurement of field effect mobility can be used to evaluate the ratio of free carriers to the number of trapped carriers.

$$\mu_{FE} = \frac{N_{GS} - N_{t,tot}}{N_{GS}} \mu_d \quad (3)$$

For AOS, the highly disordered tail states means the number density of free carriers and trapped states is a function of V_G . In crystalline Si and a-Si TFT devices the mobility increases as a function of V_G until it reaches a maximum. However in AOSs, such as

IGZO, the mobility monotonically continues to increase with increasing V_G [26]. The differences are attributed to scattering effects known in the crystalline and a-Si channel. The large overlapping s orbitals in the conduction band of IGZO are less affected by scattering effects.

Subthreshold Voltage Swing

The subthreshold swing (SS) is an important parameter for determining the minimum gate voltage required for turning on a TFT. It is defined as the voltage required to increase the current by a factor of 10 ($SS = dV_g/d \log(I_{DS})$) [13]. The SS can be used to evaluate the trap density in the AOS channel. The SS is related to the depletion capacitance (C_D), trapped interface capacitance (C_{IT}), and gate capacitance (C_g) by Equation 4 [13]. Assuming the channel is fully depleted so C_D is negligible, Equation 5 can be used to convert the interface capacitance obtained from the SS (mV/decade) as a function of trap density near the Fermi level (D_{sg}), and is given in Equation 6. Where k_B is Boltzmann's constant, e is the elementary charge, C_g is the gate capacitance, and T is the temperature (293 K).

$$SS = \left(\frac{k_B T}{e} \right) \ln(10) \left(1 + \frac{C_D + C_{IT}}{C_g} \right) \quad (4)$$

$$C_{IT} = e D_{sg} \quad (5)$$

$$SS = 59.5 \left(1 + \frac{e D_{sg}}{C_g} \right) \quad (6)$$

A lower SS indicates decreased trap state densities. A steeper transfer curve is obtained with lower values of SS indicating a higher quality channel. The value of D_{sg} is based on both trap density in the bulk channel and surface traps given in Equation 7 [80].

$$D_{sg} = \int_0^t N_{bs} dx + N_{it} = N_{bs} t + N_{it} \quad (7)$$

Sub Bandgap States

The density of subgap states (DOS) is important for understanding semiconductor performance and directly impacts TFT mobility and SS variations [81], [82]. These are states that exist within the band gap of semiconductors and can trap charge carriers leading to decrease in device performance. The density of subgap states calculated using capacitance-voltage measurements for IGZO has been found to be 1 to 2 orders of magnitude lower than in a-Si TFTs [83]. The difference in trap densities explain why IGZO has higher mobility and lower SS than in a-Si TFTs. Figure 10 shows the DOS for IGZO and their energy levels [79]. The optical band gap of IGZO is ~3.2 eV and has been determined using the Tauc relation [30], [84], [85]. The highly disordered state of AOSs gives a distribution of subgap states. Density functional theory calculations

indicate that oxygen vacancies contribute to both the shallow donor and deep donor states depending on the local atomic bonds [84].

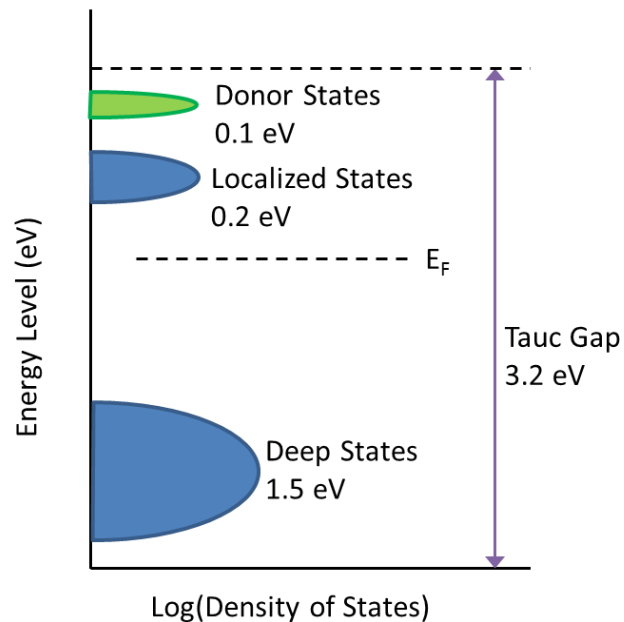


Figure 10. Summary of density of states in IGZO films and their relative energy levels. Created using literature data from [79].

Absorption spectra of IGZO shows shallow donor states, located ~ 0.1 eV from the CBM, and follow an Urbach relation ($\alpha = A \exp(h\nu/E_u)$) where A is a constant and E_u is the Urbach energy. The Fermi level is located ~ 0.2 eV below the conduction band making IGZO a n-type semiconductor [86].

The carrier concentration follows thermally activated behavior for films with carrier concentrations less than 10^{17} $\#/cm^3$ and becomes degenerate at higher carrier concentrations [85]. The degenerate states cause carrier concentrations to be independent of temperature while exhibiting thermally dependent Hall mobilities [85]. Percolation

theory suggests that when the Fermi level is located within the tail states there are potential barriers that must be overcome before electron conduction can occur [78], [87]. When the Fermi level is raised by increased carrier concentrations they are less affected by their potential barriers. Conduction of carriers at lower temperatures requires longer tortuous routes following the lowest energy barrier pathway. When thermally activated, carriers can take more direct high energy paths. Percolation theory applied to IGZO shows that narrowly distributed shallow donor states located ~ 0.1 eV under the CBM are responsible for electron transport and high mobility [27].

There is a high density of deep level DOS that are found above the valence band maximum (VBM). These deep states do not contribute to electron transport. XPS measurements of IGZO shows DOS around 1.5 eV for 9.3×10^{21} and 1.6×10^{21} $\#/\text{cm}^3$ from low and high quality unannealed films, respectively [30]. Studies on the effects of thermal annealing found a decrease in the density of deep gap states indicating that thermal annealing decreases the number of trap states near the VBM by half. The high number of DOS ($\sim 10^{20}$ $\#/\text{cm}^3$) near the VBM compared with hole densities generated by V_g ($\sim 10^{18}$ $\#/\text{cm}^3$) is the reason it is difficult to produce IGZO devices operating as p-type TFTs.

IGZO Instabilities

In order for IGZO to be used for consumer electronic devices the IGZO TFTs must have both long-term stability and reliability. Shifts in the threshold voltage or mobility can

alter the current supplied to pixels and effect brightness [88]. Sputtered IGZO films exhibit instabilities in V_{th} for prolonged gate voltage (V_g) stresses. Instabilities in AOS TFTs are attributed to charge trapping in the gate dielectric, in the bulk channel, at the channel/insulator interface, at the back channel surface, and deep acceptor traps [80]. Charge trapping in the gate dielectric can be avoided using high quality dielectrics.

Thermal annealing (200-500 °C) has been found to increase the stability of V_{th} , μ , and the SS by reducing bulk defect states [34], [86]. Annealing in inert N_2 , O_2 , and wet atmospheres has shown to have an effect IGZO TFT characteristics. Annealing in various O_2 partial pressures shows increases in mobility and decreased SS compared with devices annealed in N_2 , while annealing in a wet atmosphere further improves these parameters. These results indicate that annealing with water or O_2 further reduces trap states near the CBM by reducing oxygen vacancies [34]. Device stress tests show that changes in V_{th} can be reduced when annealed in oxygen or water atmospheres[34], [54].

Channel Thickness

Studies have indicated that threshold voltage shift depending on channel thickness [37]. IGZO TFTs with various channel thicknesses show threshold voltages from 9.1 V to 1.9 V for channel thickness from 30 to 85 nm, respectively [24]. The thickness dependent shift in V_{th} is attributed to changes in the number of carriers, which shifts positive as carrier concentration decreases [24], [35], [89], [90]. Similar behavior has been reported in amorphous HfIZO where an increase in the number of carriers results in a decreases in

V_{th} [23], [64]. Studies on IGZO TFTs using hard x-ray photoelectron spectroscopy (HX-PES) found tail states ~ 1.5 eV above the VBM, with increasing thickness [91]. The HX-PES studies indicated that the decrease in tail states is related to surface states. The O 1s core level also shifted from 0.3 to 0.4 eV with decreasing thickness indicating surface band bending. The electron mobility also increased as channel thickness increased which corresponds with increased carrier concentrations. The mobility changes are attributed to the number of free carriers and reduction of surface effects as thickness increases indicating that surface chemistry can effect TFT performance [36]. ZTO TFT devices show similar behavior with V_{th} and mobility, where the changes in electric characteristics with thinner channels were attributed to surface absorbed oxygen or water [25]. The absorbed oxygen and water are believed to act as electron donors and acceptors, respectively. Trapped charges at the back channel can play a significant role in instabilities. Atmospheric H_2O and O_2 absorbed onto the IGZO back channel can act as electron donors and acceptors, respectively [38], [65]. Absorbed molecules can alter the TFTs performance, suggesting that thinner channels can be influenced more than thicker channels. A linear decrease in the SS with increasing thickness that IGZO TFT performance is dependent on the surface [92]. Passivation of the back channel using barrier layers such as SiO_2 and SiN_x can effectively reduce instabilities in mobility and subthreshold swing. There are many studies that suggest that the performance of IGZO and other AOS TFTs are extremely sensitive to the back channel surface.

Materials and Methods

A bottom gate TFT test structure fabricated where the active channel layer can be exposed to the atmosphere. A heavily doped p-type substrate was used as the gate, and the thermally grown SiO₂ (100nm) was used as the gate dielectric. Substrates were cleaned using acetone, methanol, DI water, and blow dried using N₂. After solvent cleaning the substrates were exposed to UV-ozone (Novascan PSD Pro) for 15 minutes . The source, drain, and channel were patterned using shadow masks. The ITO (source and drain (thickness: ~160nm) were deposited first using RF magnetron sputtering using a 3 inch target with a composition of 90:10 wt. % (In₂O₃:SnO₂). ITO deposition conditions were 100 W RF power, 20 sccm Ar, and a chamber pressure of 4 mTorr. The IGZO channel was deposited on top of the source and drain using RF sputtering. IGZO was deposited using a 3 inch target with a molar composition of In₂O₃:Ga₂O₃:ZnO, at 100 W, gas flow rates of 1 sccm O₂ and 19 sccm Ar, and a chamber pressure of 4 mTorr. The thicknesses of the IGZO channel was controlled by the deposition time. The final channel thicknesses were 10, 20, 35, and 50 nm. Thickness of the source, drain, and channel layers were measured using profilometry. Two different channel width/length (W/L) ratios were examined. TFTs had the same channel width of 1000 μm and lengths of 100 or 200 μm. After deposition, the TFTs were annealed in air at 300 °C for 1 hr to improve the electric properties. Prior to applying the SAM to the back channel, the samples were rinsed using acetone, methanol, DI water, dried using N₂, and exposed to UV-ozone for 15 minutes. Octadecylphosphonic acid (ODPA) was applied by immersing the TFTs in 2 mM ODPA in 95% ethanol for 24 hours. Physisorbed SAMs were removed by

sonication for 5 minutes in 5% triethylamine and 95% ethanol and dried with N_2 .

Uncoated samples were prepared using the same method but without immersing in SAM solution.

TFT I/V transfer characteristics were measured using a semiconductor probe station (Alessi REL 4800, CascadeMicrotech) and a tungsten probe tips (Cascade Microtech). Measurements were performed by biasing the source at 0 V and drain voltage at 0.1 V for ODPAs and 1 V for FPA samples. The gate voltage was swept up and back down from -6 V to 20 V for FPA and -15 V to 25 V for ODPAs TFTs. Data was taken after multiple sweeps were performed until the transfer characteristics were stable and repeatable. Transfer curves for the different W/L ratios were compared by normalizing the drain current with the device's W/L. An example of parameter extraction from the transfer curve for a 20 nm device with ODPAs is shown Figure 11.

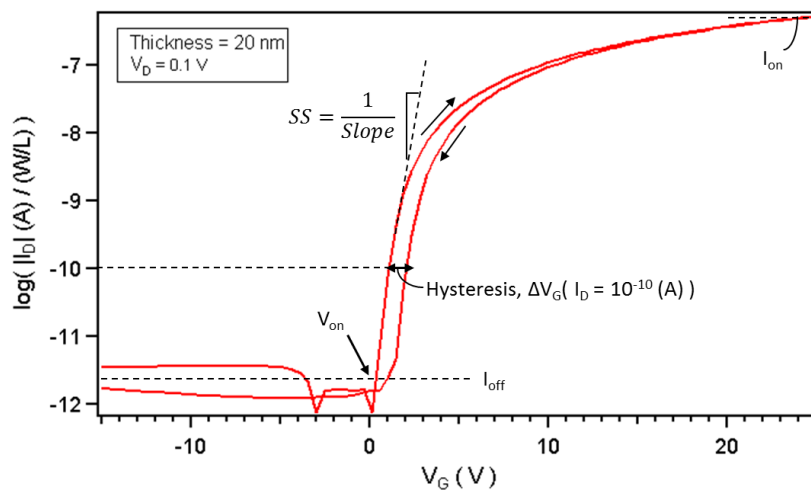


Figure 11. TFT parameter extraction from 20 nm thick channel IGZO TFT transfer curve. Arrows show the direction of V_G sweep.

V_{on} was obtained from the increase in current just below SS. SS was calculated from the inverse of the max slope. Hysteresis was calculated by the difference in V_G evaluated at a drain current of 10^{-10} (A) for the up and down V_G sweeps. I_{off} was calculated by the averaging the drain current for $V_G < V_{on}$, and I_{on} was found at the max current at $V_G = 25$ V. The average mobility was calculated using Equation 2 with a gate oxide capacitance set to 3.455×10^{-8} F/cm².

Results and Discussion

The electrical parameters of IGZO TFTs with and without ODPA were evaluated to determine how ODPA effects device performance for various thicknesses. The channel thickness of the bottom gate structure TFTs was 10, 20, 35, and 50 nm. A schematic of the final devices with and without ODPA is shown in Figure 13 a) and b), respectively. Device performance was noticeably different between IGZO TFTs with and without ODPA. Transfer curves for devices with 10, 20, 35, and 50 nm thick channels, with and

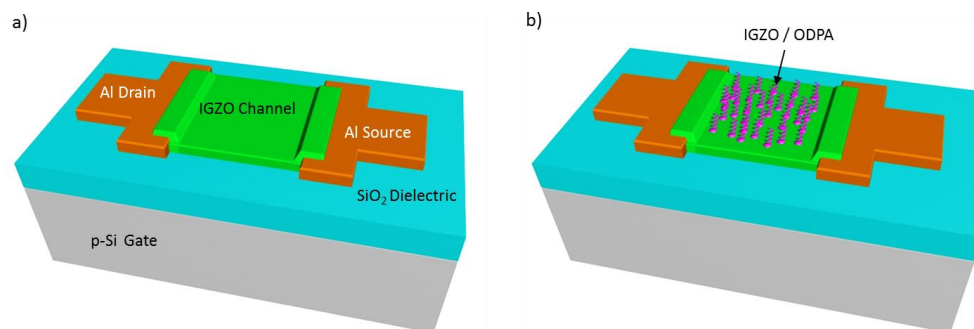


Figure 12. a) Schematic of experimental IGZO bottom gate TFT structure. b) Experimental IGZO TFT device with ODPA applied to the back channel.

without ODPA are shown in Figure 12 a-d. These curves were used for calculating V_{on} , mobility, SS, hysteresis, and I_{on}/I_{off} , which will be discussed in the following sections.

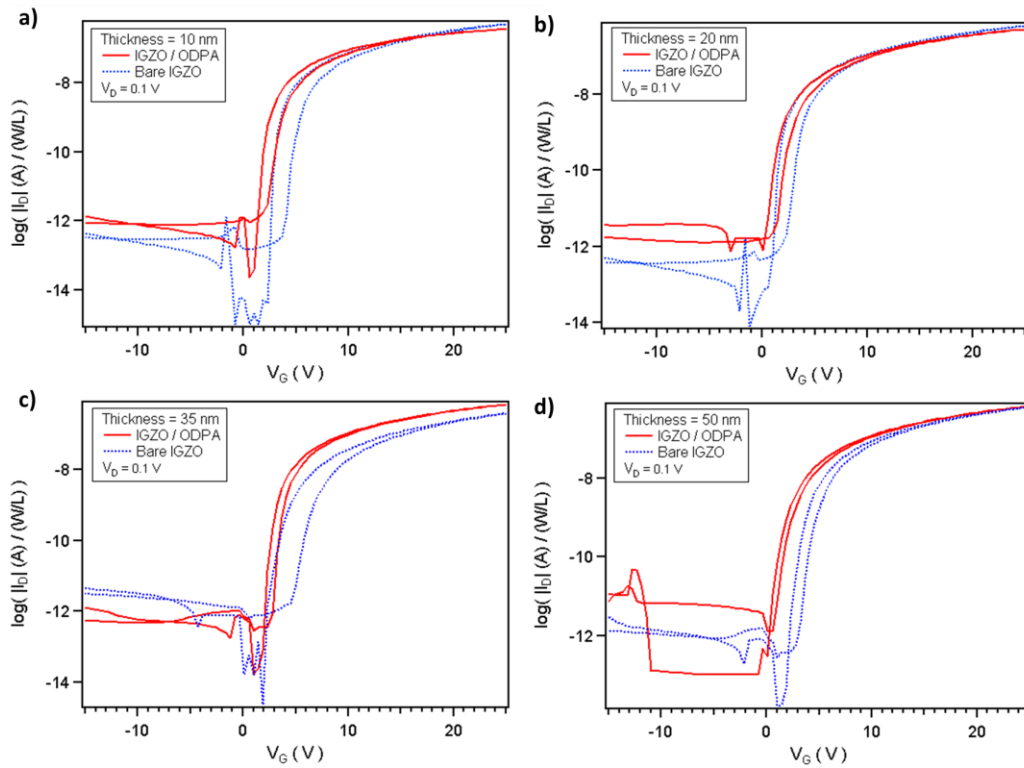


Figure 13 Transfer curves for 10, 20, 35, and 50 nm IGZO TFTs with and without ODPA. Curves show both the up and down V_G sweeps with $V_D = 0.1$ V.

Turn-on Voltage and Hysteresis

The turn-on voltage for devices with and without ODPA on the back channel is shown in Figure 14 for each channel thickness with 95% confidence intervals. As the thickness is decreased the total number of carriers in the film decreases, lowering the Fermi level, and causes V_{on} to shift positively. This is in excellent agreement with previously IGZO TFT studies [24], [35], [89].

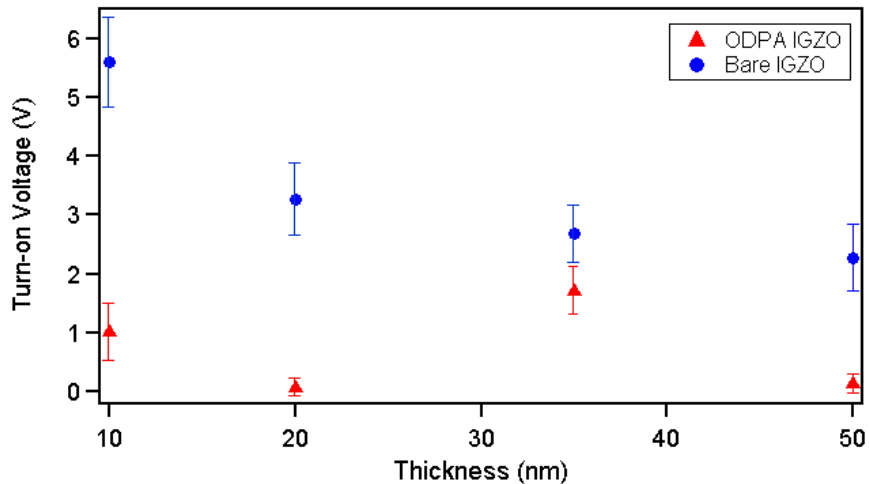


Figure 14. Turn-on voltage for devices with varying channel thickness with and without ODPA passivation. 95% confidence intervals are also shown.

It was found that IGZO TFTs with ODPA absorbed to the back surface causes a significant reduction in V_{on} compared to bare IGZO TFTs. The shift in V_{on} may be caused by band bending at the back channel as has been observed for ITO devices [47]. Increasing electron concentrations near the semiconductor back channel increases the Fermi energy and reduces V_{on} at the back channel. Another possibility is that the ODPA is acting as a donor for electron carriers causing the Fermi level to rise and lowering V_{on} . This behavior has been identified as a source of V_{th} instabilities from water and oxygen absorbing to the IGZO back channel [38], [65]. However due to the small differences in SS and mobility for devices with and without ODPA, which will be discussed later, it does not seem reasonable to attribute carrier donation to the shifts in V_{on} .

The hysteresis of devices with and without ODPA applied for different IGZO channel thicknesses is shown in

Figure 15. Device hysteresis causes variations in current between switching the device on and off for a given set of V_G . Variations in current can cause unreliable performance in the devices. Therefore it is important for hysteresis between the up and down sweeps of

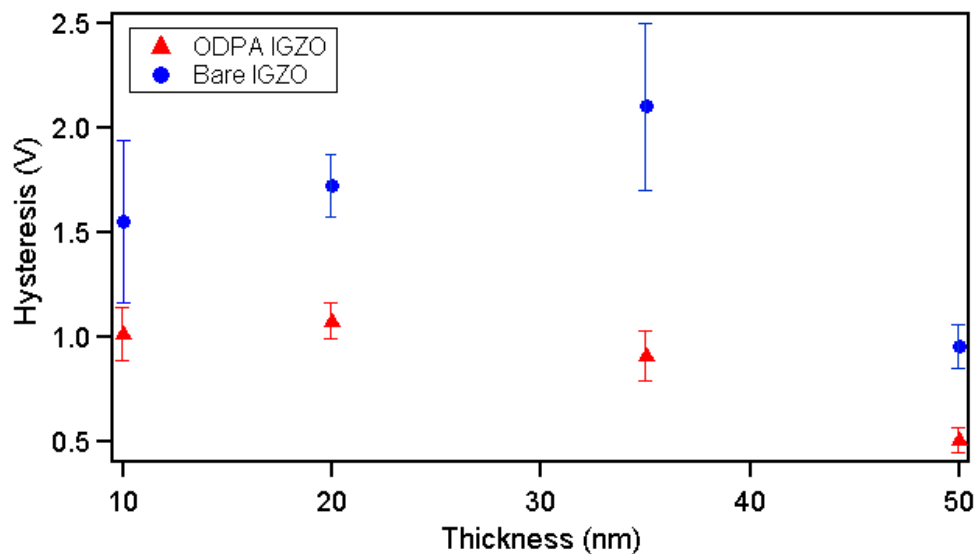


Figure 15. TFT hysteresis between V_G up and down sweeps for devices with and without ODPA on the IGZO channel surface.

V_G to be minimized to obtain the best performance.

All devices with ODPA on the back channel showed significantly lower hysteresis. Shifts in V_{th} caused by changing V_G are attributed to charge trapping at the channel interfaces, and atmospheric oxygen or water absorbed to the back channel [80]. Passivation by encapsulating the back channel using thin films such as SiO_2 or TiO_x or SAMs has been shown to reduce oxygen and water from absorbing to the back channel surface [40], [74],

[93]. It is possible that the decrease in hysteresis is due to the non-polar tail group of ODPA preventing absorption of water molecules at the IGZO back channel surface.

Subthreshold Swing and Interface Trap Densities

The subthreshold swing can be used to quantify the subgap density of defect states as shown in Equation 6. The subthreshold swing trended upwards as the channel thickness increases, with the exception of the 35 nm devices with ODPA. Figure 16 shows the subthreshold swing for devices with and without ODPA, along with 95% confidence intervals.

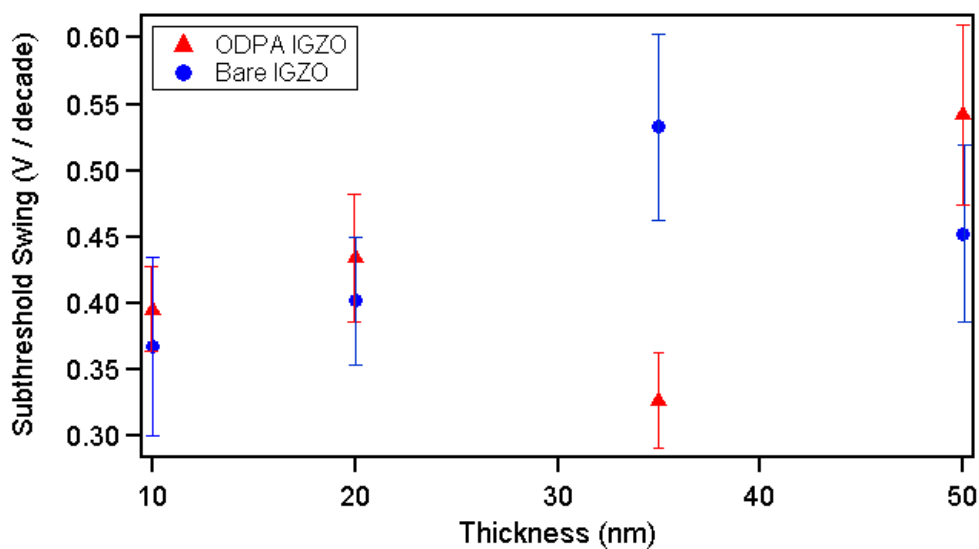


Figure 16. Subthreshold swing for various thicknesses of IGZO channels with and without ODPA. The vertical bars indicate 95% confidence intervals.

The 10, 20, and 50 nm thick IGZO devices show similar SS values indicating similar trap state densities, however a small upward trend in SS with increasing thickness was

observed. The large discrepancy for SS in the 35 nm devices may be a result from the deposition chamber. A considerable leak in the vacuum chamber was discovered after the completion of these experiments by another researcher. The leak may have allowed water and oxygen to enter the system during deposition. This could have introduced unintentional water and oxygen into the films. Oxygen vacancies in IGZO are known to create shallow donor states [26], [65]. Where water absorbed into the IGZO film can act as electron doping and can be used to stabilize IGZO by decreasing trap states [34]. The increase in SS with respect to channel thickness has been observed in IZO devices [94]. The behavior is attributed to a decrease in V_G 's influence on the back channel as thickness increases. For the IZO devices it was estimated that the majority of carriers are accumulated within 10nm of the semiconductor/dielectric interface. In thicker films the carriers must pass through more of the bulk film as they traveled from source to drain increasing the resistance [94]. The increase in bulk resistance causes the SS to increase as channel thickness increases. However, the opposite behavior has also been observed in IZO and is attributed to the reduction in the number of bulk state traps as thickness is decreased [95]. Contradicting studies have found that the SS of the IGZO devices decreases as thickness increases [24]. This is attributed to the number carriers being reduced in thinner films causing a larger percentage of carriers in trap states. At higher thicknesses (<130 nm) the SS increases, which is attributed to bulk resistance effects, similar to the IZO devices [35]. Investigations using computer simulations for IGZO TFTs estimated that the gate voltage can fully control the channel for thicknesses up to ~40 nm [96]. Above 40 nm it was found that charge shielding decreased the electric field

at the back channel. The thicknesses of IGZO investigated in this study are near or below the thickness expected for charge shielding to occur. Therefore it is expected that the gate is able to fully control the channel conductance without interference from carrier charge shielding. In contrast to previous studies, the SS has also been observed to increase as thickness increases due to the increase in the number of bulk trap states increasing as indicated in Equation 7 [65]. Devices with and without ODPA had similar subthreshold swings, but with an upward trend in SS as thickness increased. The similar SS between devices with and without ODPA suggests that ODPA does not significantly alter the trap state density in the IGZO. Equation 7 can be used to estimate the density of surface defect states in the IGZO channel using the subthreshold slope. The surface density of defect states for each thickness is shown in Table 1.

Table 1. Trap state density of IGZO with and without ODPA, calculated from the SS using Equation 7.

Surface Density of Trap States (# / cm ² eV)				
Channel Thickness	10 nm	20 nm	35 nm	50 nm
Bare IGZO	6.2E+10	7.5E+10	5.8E+10	9.2E+10
IGZO ODPA	7.1E+10	8.9E+10	1.0E+11	8.5E+10

Both surface and bulk trap states contribute to the total surface trap state density as shown in Equation 7. We find that there is little difference between trap density for IGZO TFTs devices with and without ODPA. The results indicate an increased density of trap states with increasing thickness, which is consistent with Equation 7. These results are reasonable since ODPA only resides on the surface of the IGZO channel, as such the bulk trap state density is likely unaffected.

Field Effect Mobility

The average mobility for each of the devices is shown in Figure 17. The mobility of the devices with and without ODPA are very similar for the 10 and 50 nm devices. However large variations in the data make it difficult to determine if the 20 and 35 nm devices have similar mobilities. The mobility was observed to increase from ~ 5 to ~ 8 $\text{cm}^2/\text{V s}$ as the channel thickness increases for devices with and without ODPA. This is attributed to the increase in total number of carriers in the channel as the thickness increases [24], [35], [90].

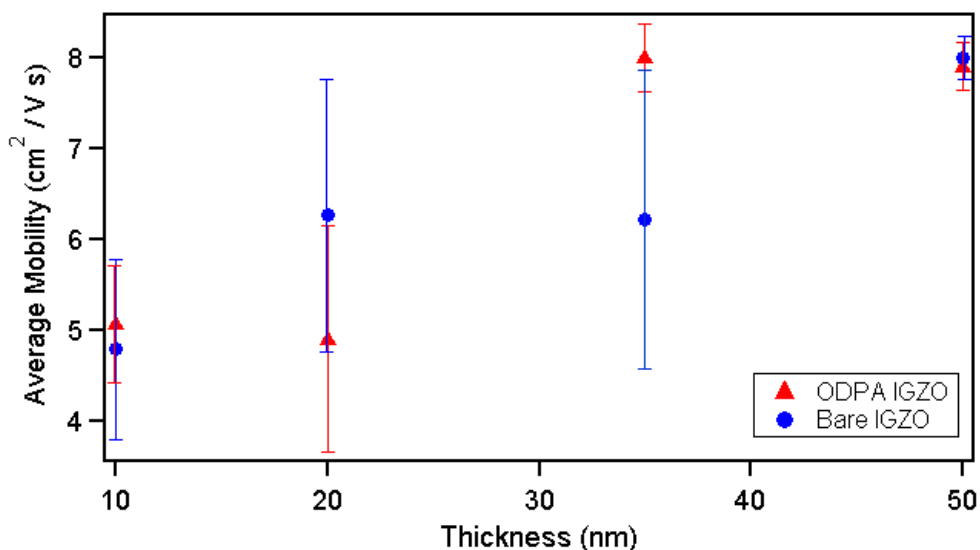


Figure 17. Average mobility of IGZO TFTs with different channel thicknesses, with and without ODPA. The bars shown 95% confidence level.

The variations in the 20 and 35 nm devices could be caused variations in carrier or defect densities incorporated during the annealing process. These may be attributed variations in oxygen and water incorporated into the films as previously discussed. The similarities between devices with and without ODPA for the 10 and 50 nm channels suggests that

ODPA does not significantly alter the ratio of free carriers to trapped carriers. Since ODPA generates a low energy surface, the adsorption of atmospheric water is minimized. Water adsorbed to the IGZO back channel is known to act as an electron donor causing shifts in carrier concentrations and altering TFT performance [97]. This would suggest that the contributions of ODPA to the channel are primary from band bending and not caused by carrier donation. A band diagram comparing the IGZO channel with and without ODPA is shown in Figure 18. In Figure 18a the conduction band minimum (E_C) and valence band maximum (E_V) shift at the SiO_2 / IGZO interface due to charge accumulation from the gate potential (V_G). The metal work function (Φ_m), band gap (E_g) and electron affinity (χ) are shown for referencing the relative energies to the vacuum level. Figure 18b shows the band structure with ODPA at the back channel interface. The dipole moment (δ_{ODPA}) created by the head group causes a shift in the conduction band near the surface [47].

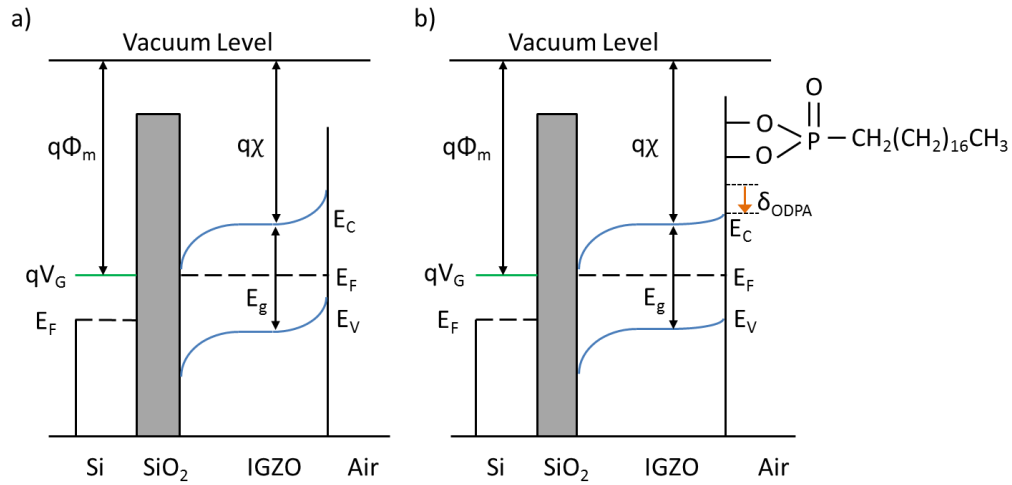


Figure 18. Band diagrams of IGZO channel in the bulk and at the dielectric and back channel interface. a) shows band diagram with bare IGZO exposed air. b) Shows the band diagram with ODPA bidentately bonded to the IGZO surface.

For ODPA, the tail group is a non-polar group, while the head group is polar. The distribution of electrons around the more electronegative oxygens causes head group to form a negative polarity with respect to the IGZO surface. While the SS and mobility are nearly the same for devices treated with and without ODPA. The constant ~ 1 V shift in V_{on} between devices with and without ODPA for all thicknesses suggests that ODPA's major contribution to variations in V_{on} is due to the ODPA dipole. The dipole of ODPA has been observed to cause a negative shift in the VBM and CBM [47]. The decrease in band bending at the back channel surface increases the electron concentration at the surface. The increased electron concentrations at surface decrease the surface trap densities.

I_{on}/I_{off} Current Ratio

The I_{on}/I_{off} ratio of the devices with and without ODPA is shown in Figure 19. The I_{on}/I_{off} ratio is similar for most of the devices. The primary difference in on/off ratios is due to variations in the off state current. The low off state current is due to the high density of deep acceptor like traps. The high density of deep acceptor traps constrains the hole carriers from becoming the majority carriers [98].

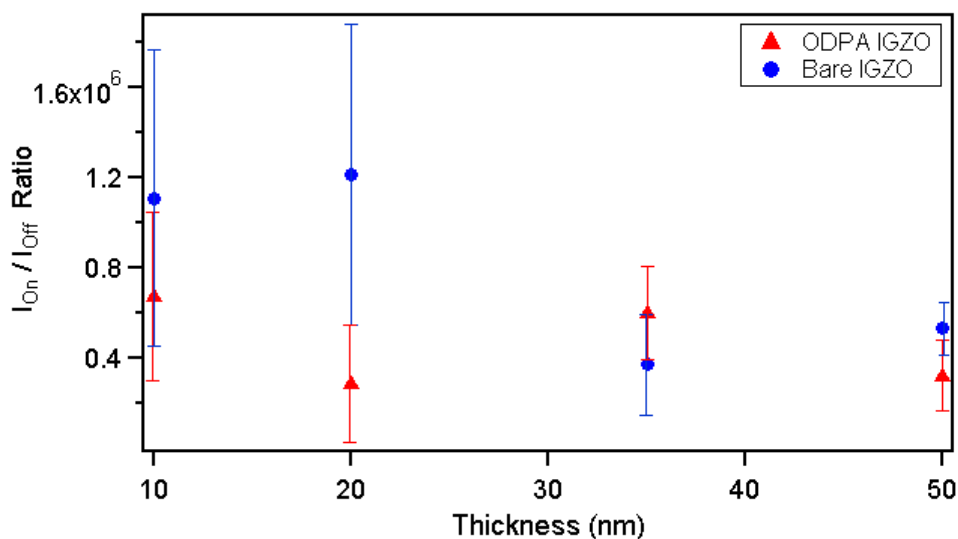


Figure 19. I_{on}/I_{off} ratio for different IGZO channel thicknesses with and without ODPA on the back channel. The bars shown 95% confidence level.

For sensor applications the back channel interaction with the analyte can lead to changes in the electronic performance. If the sensing is measured by changes in V_{on} , it is important that the interactions from the analyte are unshielded by the channel thickness. If V_G is unable to fully control the back channel, then sensitivity to the analyte on the back channel could be decreased or unobservable. Thin films for passivating the back channel may be too thick and shield the channel from electrical interactions with the

molecules of interest. On the other hand the IGZO surface needs to be protected from other molecules that may be in the same media as the analyte. The densely packed nature of SAMs can help passivate the surface from interference of other molecules. This has been successfully demonstrated for passivating against absorbed atmospheric water and oxygen [38], [66], [93]. SAMs allow for highly customizable surfaces that can directly influence the underlying IGZO channel properties. The electrical sensitivities of thin IGZO channels to their environment coupled with tailored SAMs can be a cost effective method for developing field effect sensors.

Chapter 4: Patterning of IGZO Thin Film Transistors Using Electrohydrodynamic Ink Jet Printing

Introduction

Electrohydrodynamic ink jet printing (EHDP) can be used to fabricate circuits by depositing functional inks [99]–[101]. EHDP is an effective non-contact method for depositing materials below the resolution limits of traditional printing, such as thermal and piezoelectric inkjet printing. Printed features using EHDP can vary from micron to submicron scale [50], [101], [102]. Typical drop on demand (DOD) thermal and piezoelectric printing methods are limited to feature sizes of $\sim 30\ \mu\text{m}$ with a droplet volumes $\sim 1\ \text{pL}$, although larger features are much more common [48]. Microelectronics manufacturing requires producing feature sizes on the micro to nano scale. The resolution of traditional printing methods limits their use to applications with larger features ($>30\ \mu\text{m}$). EHDP can be utilized for fabrication of microelectronic components with smaller features ($<30\ \mu\text{m}$). Direct patterning of materials allows for reduced waste compared to commonly used photolithography. The cost of materials such as, precious metals, functional polymers, and enzymes can be significant. The cost of production can therefore be reduced by reducing the amount of materials needed to pattern. Printing is advantageous for rapid patterning of precise amounts of functional materials. EHDP has been used for depositing precise amounts of enzymes for biosensors, and ibuprofen for drug delivery systems [20], [52], [103]. High resolution patterns achieved with EHDP allow for direct patterning of micro and nano scale features. For example, EHDP deposition or patterning of inorganic materials is also of much interest. Micro wires (25-

100 μm) using silver and copper nano particle inks have been demonstrated [101], [104]. Quantum dot inks have been deposited with line widths of 25 nm [50]. Since the process is a noncontact approach, there is minimal risk of contamination from the nozzle to the substrate. Contamination is a serious issue for producing patterns of high quality thin films and biomedical materials such as proteins and drugs. IGZO semiconductors have been shown to be an excellent candidate for display applications. A single pixel is composed of at least 3 sub-pixels that control red, green, or blue light; each sub-pixel is controlled using a TFT to control the orientation of the liquid crystal in liquid crystal displays. A schematic of a liquid crystal display pixel is shown in Figure 20 [105].

In order for pixel density to be high enough for high resolution displays, the TFTs and other components needs to be considerably smaller than the pixel. Current Mac Book Pros using Apple's Retina displays utilizing IGZO TFTs have 227 pixels per inch [106]. An image showing pixel size in a pixel array from Samsung's Super-AMOLED display used for the Samsung Galaxy S4-mini is shown in Figure 21. The display features 256 pixels per inch [107]; with an approximate pixel length and width of 100 μm .

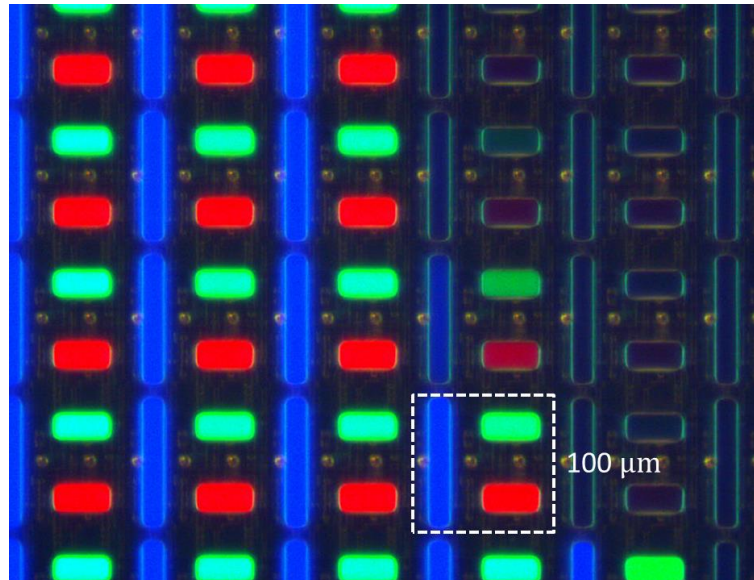


Figure 20. Pixel and subpixel array for the Samsung Galaxy S4 Mini. "Samsung SuperAMOLED : weekend die-shot" (c) by ZeptoBars, retrieved from <http://zeptobars.ru/en/read/Samsung-SuperAMOLED-TFT-display-Galaxy-S4-mini>, used under Creative Commons Attribution 3.0 Unported. Image was modified to include dotted outline and "100 μm"

The features, such as electrodes and channel, of the TFTs must be much smaller than the pixel which require high resolution patterning techniques such as photolithography. Traditional printing methods are unsuitable for high resolution display manufacturing due to the resolution limits previously discussed. However, EHDP has the resolution required for patterning TFTs in displays.

Electrohydrodynamic Ink Jet Printing

Electrohydrodynamic ink jet printing is achieved by applying an electrical field between the print nozzle and substrate. The electric field draws ions in the fluid to the surface of the meniscus. At elevated voltages the meniscus of the fluid deforms into a cone-like

structure, known as a Taylor cone [49]. At a sufficiently high potential the ionic repulsion at the Taylor cone tip overcomes the surface tension and a droplet is ejected. Various droplet ejection modes can be obtained by varying printing parameters such as voltage bias, voltage pulse height, pulse time, and pulse frequency. The different ejection modes are drip, micro-drip, jet, spindle, and spray [108]–[110]. Figure 22 shows how voltage pulse amplitude effects the generated printing mode [110]. As can be seen in Figure 22, droplets formed from the tip of Taylor cone can be considerably smaller than the diameter of the nozzle.

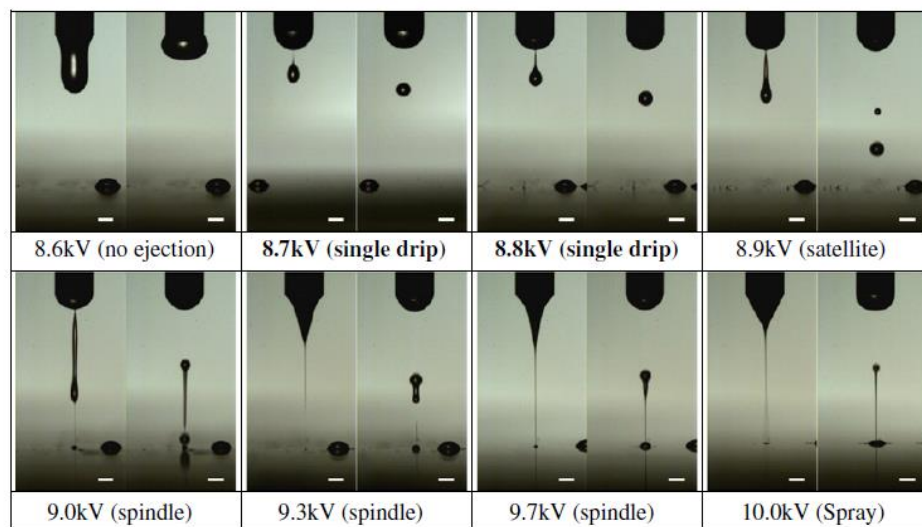


Figure 21. Different droplet ejection modes generated by varying the voltage pulse amplitude. Note the droplet size difference between droplet and nozzle diameter. "Reprinted from J. Aero. Sci., 46, M.W. Lee et al., A study of ejection modes for pulsed-DC electrohydrodynamic inkjet printing, 1-6, Copyright (2012), with permission from Elsevier."

Drip and microdrip are characterized by a single droplet being ejected for each voltage pulse [110]. Spindle mode generates elongated droplets. Spindle mode occurs at higher voltage pulses than drip mode or when the pulse time is long [109]. Spray mode occurs at

the highest electric pulses, where the high ionic repulsion causes the multiple droplets to break from the Taylor cone, forming a spray [110]. The desired printing regime used for study was drip mode. Drip mode generally exhibits the greatest control over precise and discrete droplet placement.

Droplet formation in thermal and piezoelectric printers is governed by nozzle size and fluid velocity, viscosity, and surface tension [48]. Spreading of the droplet on the substrate influences the final deposited resolution [111]. These interactions limit the feature size of traditional printing methods to $\sim 30 \mu\text{m}$ with a droplet diameter of $\sim 2 \mu\text{m}$ [48]. Lowering the viscosity and surface tension of functional inks to achieve smaller printable droplets is not always desirable as it may impact the final material properties. The printing mechanism of EHDP allows printing of finer droplet sizes while using inks that normally would not be possible using printing methods such as piezoelectric, thermal, and screen printing.

A widely used method for micro and nano patterning of electronic devices is photolithography [16]. Photolithography requires specialized photosensitive materials and complex optical tools [16]. To further complicate the process, the wavelength of radiation needs to be narrowly distributed and typically smaller than the desired feature sizes which require higher energy light sources. The use of photolithography equipment can be avoided by directly depositing resist materials using DOD printing techniques. In this thesis a polymer based photoresist, SU-8, was crosslinked using thermal heating

making it suitable for patterning without photon induced crosslinking. SAMs can offer an alternative to photoresists as etch resists. SAMs readily attach to the surface of oxides and metals to form a self-limiting monolayer. The SAMs can be tailored to include tail groups that are hydrophobic or hydrophilic allowing the surface to be functionalized. The functionalized surface can act as an etch protectant allowing for selective etching of materials. The resist is removed after etching to produce the final desired pattern.

EHDP was used for indirect patterning of the IGZO TFT channel and will be the focus of this chapter. Indirect patterning of IGZO is achieved by depositing materials to act as etch resists directly on top of a blanket film of IGZO. Once the pattern is formed by etching, the resist is removed to produce the desired material in specific regions. EHDP can be used in place of photolithography to directly pattern etch resists. EHDP is advantageous over traditional printing methods for micro and nano fabrication due to the higher resolution that can be obtained with a wide range of fluid properties. Here micron wide channels are formed in IGZO TFTs using EHDP. The micro channels are realized by first depositing IGZO, followed by the patterning of an etch resist. The IGZO sample is then etched in regions not protected by the resist using an etchant, such as HCl. Both printed traditional photoresist, SU8, and the self-assembled monolayer, n-hexyl phosphonic acid (HPA) are demonstrated as etch resists in these studies. The electrical performance of IGZO TFTs patterned using HPA and SU8 were evaluated using I-V electrical measurements described in Chapter 2. The parameters obtained from the I-V measurements were used to evaluate the quality and effects of EHDP patterning.

Literature Review

Electrohydrodynamic Ink Jet Printing (EHDP)

The phenomena of fluid ejection under the influence of an electric field was first studied in 1964 by Sir Geoffrey Taylor [49]. When a fluid in an open capillary has an electric field applied, the ions collect at the surface of the meniscus. The Coulombic forces deform the meniscus to form a cone as shown in Figure 23. The field induced cone is referred to as a Taylor cone [49]. The static Taylor cone in a constant field can be described as a point of equilibrium between surface tension forces (F_γ), hydrodynamic forces (F_h), and ionic forces (F_E) [49], [108].

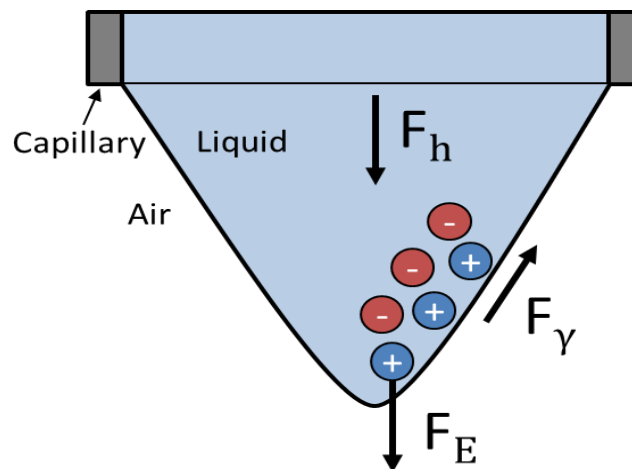


Figure 22. Forces induced on a fluid in the presence of an electric field at the tip of a needle.

When enough ions are concentrated at the tip of the Taylor cone by applying a sufficient electric field, the repulsive ionic forces overcome the surface tension forces and a

charged droplet is ejected [49]. The ejected droplet is accelerated towards the substrate by the applied potential. Generally, pressure is applied to the back of the needle to continuously supply fluid from the fluid reservoir to the needle tip [112], [113]. The flow rate of the ejected fluid under a constant potential follows a Poiseuille-type relation and is given by Equation 8 [114]. Where Q is the flow rate, ΔP is the pressure drop, μ_{liq} is the fluid viscosity, ϵ_0 is the permittivity of free space, γ is the surface tension, E is the magnitude of electric field, d_n and L are the diameter and length of the nozzle, respectively.

$$Q \approx \frac{\pi d_n^4}{128 \mu_{liq} L} \left(\Delta P + \frac{1}{2} \epsilon_0 E^2 - \frac{4\gamma}{d_n} \right) \quad (8)$$

It can be seen that the flow rate is dependent on the electric field squared. Variations in the height between the tip and substrate can alter the electric field strength and substantially change flow rates. To better control the droplet generation frequency, a constant DC bias combined with a pulsed voltage scheme has been employed [115]. The constant bias is used to maintain the static Taylor cone, while the voltage pulse generates a droplet. The optimized frequency of pulsed voltage leads to stable control in the desired printing regime.

Many different ejection modes can be achieved depending on the voltage applied. Among the modes are drip, micro-drip, cone-jet, spindle, and spray [109]. Cone-jet is classified by a continuous fine stream of fluid extending from the tip to the substrate. Spindle mode

is similar to drip mode but the ejected fluid exhibits an elongated shape. Spray mode is achieved at the highest voltages and a fine mist of multiple droplets is ejected. In drip mode the ejected droplet is circular in shape. Drip mode produces uniform droplets that are desirable for uniform drop on demand printing. While operating in drip mode, continuous lines can be created by overlapping of uniform discrete droplets. Careful control over the printing conditions and parameters allow for maintaining the desired mode.

Lithography

Photolithography is a commonly used for the production of TFTs and other micro-electronic structures [16]. The photolithography steps require high energy, complex optics, and intensive radiation exposures which contribute to high manufacturing costs [58]. In photolithography the substrate is coated with a photosensitive material, known as photoresist, which changes solubility when exposed to radiation. A mask is placed over the photoresist to selectively expose regions to radiation. The soluble regions are removed using solvent, usually known as developer, to expose the substrate. An etchant is then used to remove the exposed regions of the substrate while the regions covered with photoresist remain unetched. The industrial photoresist used for these studies is SU8, a negative tone resist [116]. Normally i-line radiation (365 nm) is used to cross link SU8 and render exposed regions insoluble. However, SU8 can also be crosslinked by annealing above 150 °C [116, p. 8]. Since printing SU8 directly transfers the desired pattern to the substrate the crosslinking can be achieved by thermal annealing, thereby

avoiding the radiation exposure step; ultimately the manufacturing costs of displays may be reduced, leading to cheaper consumer electronics.

Self-Assembled Monolayers

An alternative to patterning with photoresists is to use self-assembled monolayers to form an etch resist. Long alkyl chains with phosphonic acid tail groups such as n-hexyl octadecyl phosphonic acid (ODPA) and phosphonic acid (HPA) have been found to reactively bond to oxygen on metal oxide surfaces [45]. Phosphonic acid SAMs have been found to form mostly bidentate bond, densely packed monolayers on ITO and SnO surfaces [47], [117], while the primary binding mode on ZnO has been found to be tridentate [44]. The n-hexyl phosphonic acid SAMs with alkyl chains form densely packed monolayers creating a surface with hydrophobic properties. Chemisorbed octadecyl phosphonic acid patterned IGZO by micro contact printing has been found to create a layer resistant to etching by aqueous oxalic acid [118]. In this study, HPA deposited using EHDP was used for the patterning of micro wires for the IGZO channel. After the etching process the SAM can be effectively removed from the oxide surface with an oxygen plasma [44], [118].

Materials and Methods

Printing of etch resists was accomplished using the electrohydrodynamic ink jet system described in Chapter 2. In order to achieve sub 30 micron printed features, both the ink properties and EHDP printing parameters were optimized. Individually printed droplets

were deposited by applying constant needle bias with a square pulse. The constant bias is important for maintaining the fluid meniscus in a Taylor cone. Pulsing the voltage allows for controlling and stabilizing the droplet ejection frequency.

SU8 Ink Formulation

The SU8 ink was modified in order for it to be printable using EHDP. Many concentrations of SU8-2000 (MicroChem) diluted in cyclopentanone (Sigma Aldrich) were investigated to determine the optimal ink formulation. The viscosity of the stock SU8 created too much resistance to flow through the narrow 5 μm diameter nozzle. The stock SU8 had a solids weight concentration of 30% and a viscosity of 7.5 cSt [116]. To reduce the viscosity the SU8 was diluted in cyclopentanone. Solid concentrations of 0.5% and above produced thin long streams or elongated droplets that made controlling the printing difficult. It is likely that the higher concentrations flow with non-Newtonian visco-elastic properties making it difficult for droplets to break off [119]. It is important to use the highest concentration possible to be able to deposit SU8 thick enough for it to adequately protect the material during the etch step. The optimal concentration that we found was a dilution ratio was 1:200 (SU8:cyclopentanone), corresponding to 0.15% (wt) of solids. The addition of the surfactant Triton-X 100 (Sigma Aldrich) was also evaluated to modify droplet formation. Concentrations of 0.1-0.001% with Triton-X 100 caused the droplets spread non-uniformly on the IGZO surface and was decided to be undesirable.

HPA Ink Formulation

The self-assembly of HPA on oxide surfaces can be used to modify the IGZO surface to make it hydrophobic. The deposited HPA can serve as a hydrophobic etch resist for dilute HCl etchant. Ethanol was chosen as the solvent due to its ability to fully dissolve solid HPA in the concentrations of interest. A range of concentrations of HPA in ethanol (1-10 mM) were examined to determine the optimal concentrations. Solutions were stirred for 5 minutes and then sonicated for 2 minutes to ensure good dispersion of HPA in the ink, while concentrations above 5 mM caused precipitates to form in the bulk solution after 24 hours. Concentrations above 3 mM resulted in nozzle clogging due to the formation of precipitates at the tip of the nozzle. It is likely that solvent evaporation at the nozzle increases the local concentration of HPA at the tip resulting in precipitate formation. Lowering the HPA concentration to 1 mM effectively prevented precipitation at the tip of the nozzle, and was used for patterning the IGZO channel.

Printing Etch Resist Inks

The EHDP parameters for both the SU8 and HPA inks were systematically varied to identify the optimal parameters for controllable and reproducible droplet placement. The conditions required to form a Taylor cone were determined by first using DC operation without the voltage pulses. By using DC operating, the voltage threshold to form a stable Taylor cone with and without droplet ejection was obtained. Determining the proper distance from the nozzle to the substrate is critical to obtain uniform droplet sizes and placement. Generally longer distances (>500 μm) produce droplets with more variation in

their placement on the substrate. Non-uniform placement resulted in producing lines with higher line edge roughness. A distance of 200-500 μm was found to produce the least variation in droplet placement. The distance from the tip to the substrate needs to be small ($<500 \mu\text{m}$) in order to obtain a high electric field strength. The optimal height of the needle tip above the substrate was determined by applying a constant bias and observing the height at which droplet generation occurs. By keeping a close distance the distribution of droplet placement could be readily controlled. Once the threshold bias and height was determined, the voltage pulse height was varied (20-300 V) to determine the ideal voltage pulse required to eject a single droplet. The voltage pulse frequency was varied from 1-200 Hz to determine the optimal frequency for producing the smallest lines. Printed lines were achieved by moving the stage to create overlapping of the ejected ink droplets. Printing parameters for each ink were optimized to produce the minimum uniform line widths possible.

Microscope images of printed SU8 and HPA on IGZO are shown in Figure 24 a and b, respectively. Printed lines of SU8 was performed using a 5 μm diameter needle and resulted in 4 μm wide lines. Printed lines of HPA was performed using a 1 μm diameter needle and resulted in 4 μm wide lines.

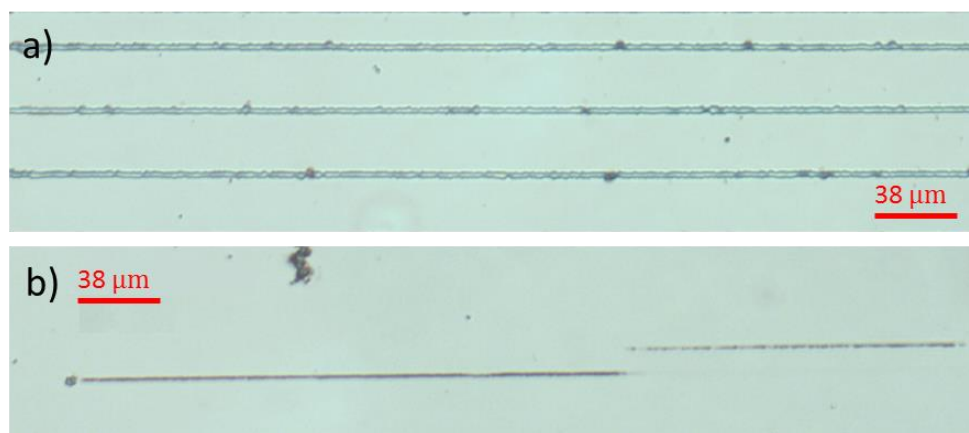


Figure 23 Optical image of IGZO substrate with printed a) SU-8 and b) HPA lines with a line width of 4 and 2 μm , respectively

TFT Fabrication

The SU8 and HPA inks were printed using EHDP to define micron scale features of the IGZO channel. Shadow masks were used to roughly deposit the sputtered materials at the mm scale. First, square (750x1000 μm) IGZO pads, 50 nm thick, were sputter deposited onto heavily doped p-type Si with 100 nm of thermally grown SiO_2 . 50 nm of IGZO was sputter deposited using a 3 inch target with a molar composition of $\text{In}_2\text{O}_3:\text{Ga}_2\text{O}_3:\text{ZnO}$, at 100 W, gas flow rates of 1 sccm O_2 and 19 sccm Ar, and a chamber pressure of 4 mTorr. Before deposition and patterning the samples were rinsed using acetone, methanol, water, and blow dried under N_2 for 30 seconds. The samples were then exposed to UV-ozone (Novascan PSD Pro) for 15 minutes. EHDP was used to print 4 and 2 micron wide lines of SU8 and HPA ink, respectively, onto the IGZO surface. Samples patterned with SU8 were annealed on a hot plate in ambient atmosphere at 95 $^\circ\text{C}$ for 5 minutes to crosslink the photoresist prior to etching. Etching of the IGZO was performed by immersing the

patterned samples in dilute HCl (1:200, HCl:H₂O) for 25 seconds. After etching the SU8 was removed using SU8 developer and exposed to (50 W) oxygen plasma for 2 minutes to remove residual SU8. The printed HPA was removed by oxygen plasma (50 W) for 2 minutes. An example of the patterning process using SU8 and a 30 micron diameter needle is shown in Figure 25 a-c.

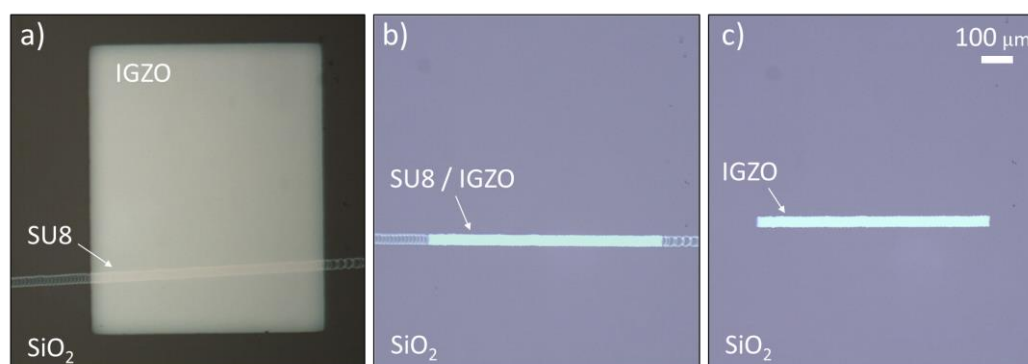


Figure 24. Optical microscope images of EHDP IGZO patterning process. a) SU8 printed on IGZO pad. b) SU8 and IGZO post etch. c) SU8 removed with only IGZO channel remaining. Channel width in these images is $\sim 25\mu\text{m}$ and length $\sim 750\mu\text{m}$.

After etching the IGZO samples were annealed in a tube furnace in ambient atmosphere, at 300 °C for 1 hour. Aluminum source and drain were deposited and patterned using thermal evaporation and a shadow mask. The final channel length between the Al source and drain was 100 µm. Figure 26 shows a 2 µm wide line of printed HPA on the IGZO films. The final HPA patterned device with source and drain deposited is shown in Figure 26c. Figure 26b shows a 4 µm wide line of printed SU8 on an IGZO film. The final device patterned by printed SU8 is shown in Figure 26d. The thickness of the IGZO channel was measured post patterning using a profilometry. The final channel thickness was $\sim 50\text{ nm}$.

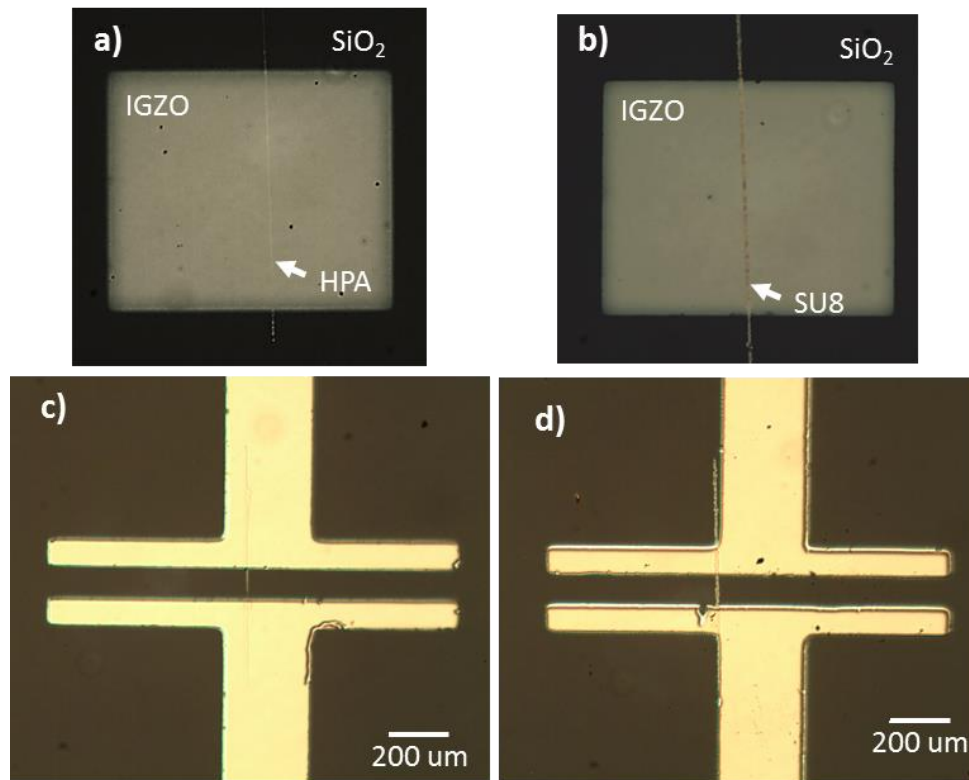


Figure 25. Microscope images of printed lines on IGZO using a) HPA and b) SU-8. Final devices with etched IGZO and Al source and drain patterned using c) HPA and d) SU-8. c) The width of the HPA patterned channel is $\sim 2 \mu\text{m}$. d) the width of the SU8 patterned channel is $\sim 4 \mu\text{m}$.

TFT Transfer Characteristics

Transfer characteristics were carried out to assess the electrical performance of microchannel TFTs using a semiconductor probe station (Alessi REL 4800, CascadeMicrotech). A schematic of the TFT and the probe locations is shown schematically in Figure 27. Electrical measurements were made by contacting the Al source (V_S) and Al drain (V_D) electrodes, and the Si gate (V_G) was made by scratching through the SiO₂. Measurements were carried out with constant $V_D = 1 \text{ V}$ and $V_S = 0 \text{ V}$.

The current through V_G , V_S , and V_D was measured as V_G was swept from -10 to 30 V and back from 30 to -10 V at a rate of 500 mV/s. The gate voltage was swept 15 times to obtain stable I-V curves. It was found that the I-V sweep curves no longer changed after 5-7 sweeps. The turn-on voltage, hysteresis, mobility, subthreshold swing, and I_{on}/I_{off} ratio for EHDP patterned IGZO TFTs were calculated using the methods described in Chapter 2.

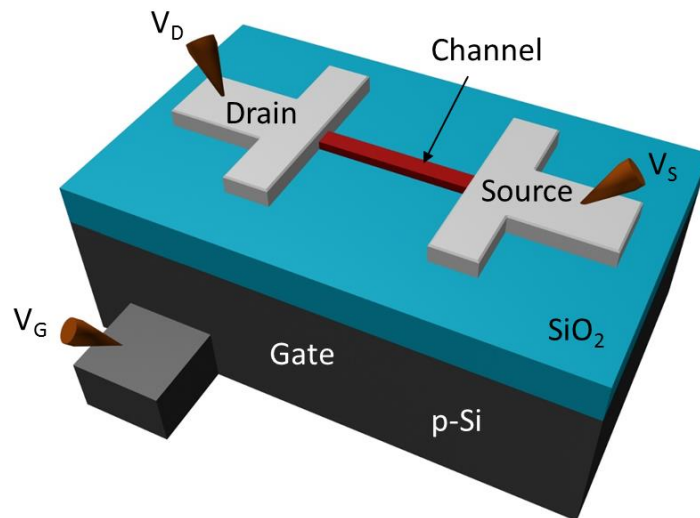


Figure 26. Schematic of EHDP patterned IGZO TFT. Probes for the source, drain, and gate were connected at V_S , V_D , and V_G respectively.

Results and Discussion

HPA Patterned IGZO

EHDP was utilized to produce printed HPA ink with feature sizes $\sim 2 \mu\text{m}$. Ethanol containing 1 mM HPA produced the best line resolution and repeatability. The resolution of the features was determined primarily by needle diameter. The diameter of the printed droplets decreased as nozzle diameter was decreased. Typical line widths obtained using various needle diameters are shown in Table 2. The HPA lines using the 1 μm diameter needle were larger than 1 μm . This is due to the droplets wetting the substrate, which results in larger features than the needle diameter or the droplet diameter.

Table 2. Printed line widths using various needle diameters.

Needle Diameter (μm)	Printed Line Width (μm)
30	60 – 25
5	30 – 5
1	5 – 2

Stable drip mode was achieved using pulse heights of 50-100 V. The thinnest HPA lines were achieved using an electrical bias of 350 V and a pulse height of 50 V. We found that the voltage alone was not enough to continuously draw ink through the thin capillary, thus pressure was applied to the back of the needle to supply a continuous flow of ink to the tip of the needle. A pressure of ~ 1 psig was sufficient to deliver ink to the tip of the 1 μm needle. Increasing the pulse frequency decreased the droplet size and subsequent line width. Figure 28 shows HPA lines printed on IGZO using a 5 μm diameter needle with

varying frequencies. The line width decreases from 28 to 17 μm as the frequency was varied from 40 to 100 Hz, little change was observed between 100 and 200 Hz.

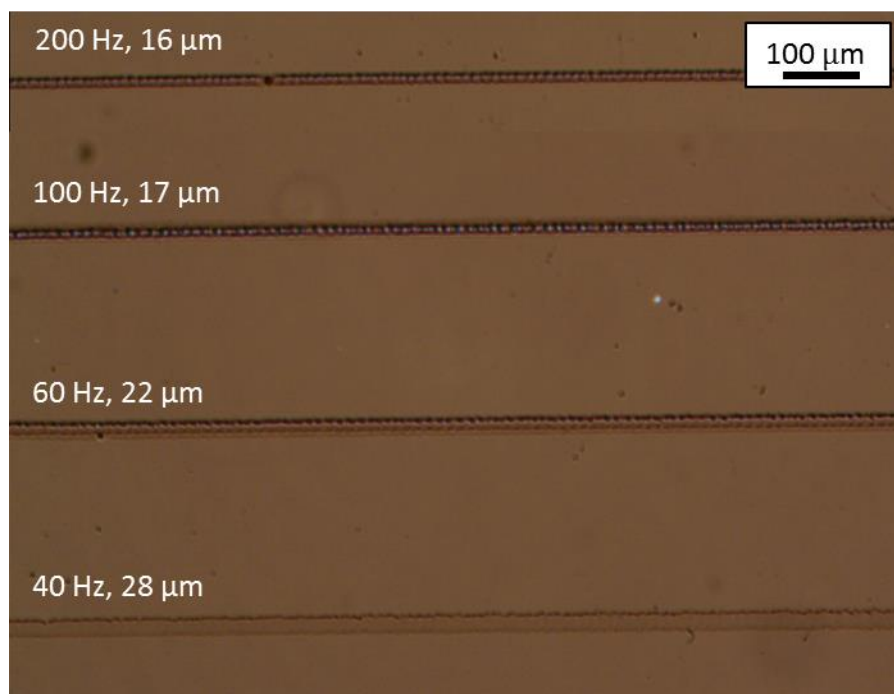


Figure 27. Changes in printed HPA line width as pulse frequency is varied. Line widths shown are 17, 17, 22, and 28 μm for 200, 100, 60, and 40 Hz, respectively. Bias = 350 V, pulse height = 100, pressure = 0.5 psig, needle diameter = 5 μm . Stage velocity was held constant at 0.12 $\mu\text{m}/\text{s}$.

The droplet size dependence on frequency can be explained by the duration of the pulse which influences the concentration of ions in the Taylor cone. Shorter pulse durations concentrate fewer ions in the Taylor cone and generates smaller ejected droplets [120]. The optimal parameters for printing 2 μm features of HPA are provided in Table 3.

Table 3. EHDP printing parameters for producing 2 μm features using HPA ink.

Ink	Bias (V)	Pulse Height (V)	Pulse Frequency (Hz)	Height (μm)	Nozzle Diameter (μm)	Pressure (psig)
HPA	350	50	100	100	1	1

Using the parameters from Table 3, 2 μm uniform lines could readily be printed using EHDP. The deposited HPA successfully formed a protective surface that was resistant to etching in the dilute HCl solution.

SU8 Patterned IGZO

Similar methods used for the HPA ink were used to determine the optimum printing parameters for the SU8 ink. The SU8 ink, SU8 2000 was diluted in cyclopentanone at a ratio of 1:200. This dilution corresponded to a solids concentration of 0.15% (wt). The concentration was found to greatly influence the minimum resolution that could be achieved using EHDP. Drip mode printing was not achievable for solids concentrations greater than 1% (wt). Concentrations greater than 1% (wt) were printable as a continuous jet but the minimum obtained feature size of 1% (wt) was 20-30 μm . Drip mode operation was obtainable for concentrations in the range of 0.15-0.5% (wt) with features size increasing with increasing concentration. Inks with 0.3% could regularly print individual droplets and lines with diameters and widths of 10-20 μm while using a 5 μm diameter needle. While SU8 diluted to 0.15% (wt) was able to produce 4-5 μm lines. There are numerous possible reasons for the dependence of resolution on SU8

concentration. Increased solids in the ink could cause the droplet to elongate prior to breaking free of the Taylor cone. Solvent evaporation may increase the monomer concentration at the ink surface. Crosslinking SU8 can be initiated by UV radiation (350-400 nm) [116]. UV radiation from ambient light may initiate polymerization at the tip of the needle causing the viscosity to increase. Visco-elastic fluids exhibit a time dependent relation time that makes high speed droplet formation difficult. Elongated necking extending from the droplet to the meniscus is commonly observed for drop on demand printing of visco-elastic polymers [119]. By increasing solvent content in the ink the degree of unwanted polymerization can be minimized. Another factor contributing to wider line widths may be the high wettability of the SU8 ink on the outer surface of the Au/Pd coated needle. Even though the Au/Pd was coated with 1H,1H,2H,2H-perfluorodecanethiol to increase the contact angle and decrease wetting of the outer surface of the needle, excessive back pressure or voltage caused the SU8 to wet and spread on to the exterior of the needle. This problem became worse without the use of the 1H,1H,2H,2H-perfluorodecanethiol. A better surface treatment could improve resolution by restricting the diameter of the meniscus to the interior of the nozzle. Low temperature heating the SU8 ink to reduce the viscosity and increase flow rate could also assist in printing finer resolution at higher concentrations. This heating would need to be below 80 °C to prevent unwanted crosslinking in the needle [121]. Reducing the viscosity by heating was not examined because the EHDP system lacked ink reservoir heating capabilities.

The EHDP electrical parameters required to print 4 μm features of SU8 were much higher than what was required for printing HPA. The optimal voltage bias was 600 V with a pulse amplitude of 150 V. One reason for the higher voltages is due to the increased distance between nozzle and substrate. A distance of 400 μm was necessary to obtain stable printing. At shorter distances the Taylor cone would extend very close to the substrate and minor deviations in conditions would cause large instabilities in the printing regime. A back pressure of ~ 0.5 psig was used for printing SU8. The required back pressure was lower than the HPA ink since the 5 μm diameter nozzle was much larger than used for HPA (1 μm diameter). A summary of the optimal printing parameters for SU8 in cyclopentanone diluted to 0.15% (wt) solids is provided in Table 4.

Table 4. EHDP printing parameters for producing 4 μm features using 0.15% (wt) SU8 in cyclopentanone.

Ink	Bias (V)	Pulse Height (V)	Pulse Frequency (Hz)	Height (μm)	Nozzle Diameter (μm)	Pressure (psig)
SU8	600	150	60	400	5	0.5

Figure 29 shows continuous 4 μm wide SU8 lines printed using EHDP. From the optical microscope image the line edge roughness is significant. The high edge roughness may result from how the ink interacts with the substrate. Small variations in surface energy can modify how SU8 wets the IGZO surface causing edges that are not smooth.

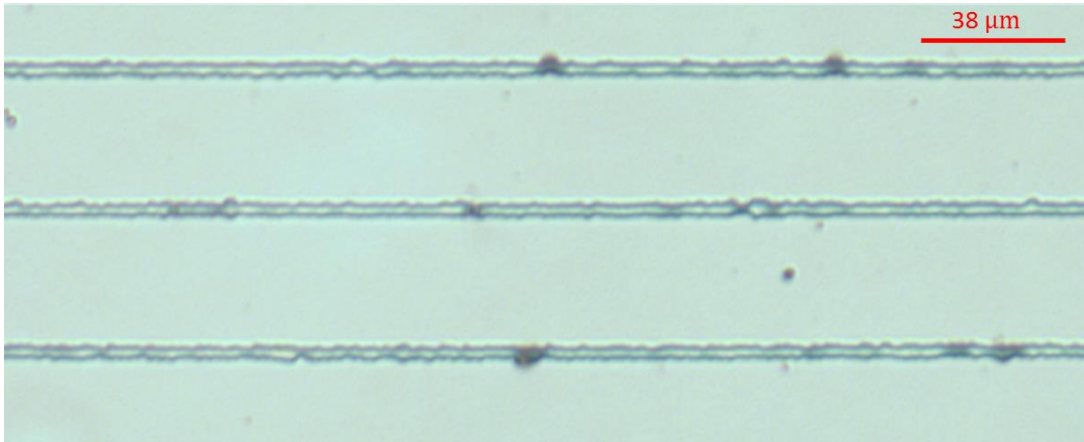


Figure 28. Optical microscope image of 4 μm wide lines printed with SU8 on IGZO surface.

Alternative surface cleaning treatments such as oxygen plasma or sonication in solvents could help decrease the edge roughness by reducing variations in surface energies caused by surface contamination. Another possible explanation for the rough lines is from droplet size variation. If the size of the droplets varies the surface coverage would also vary causing rougher line edges [48].

EHDP Patterned IGZO TFT Performance

For EHDP printing HPA ink to be considered as an alternative path for patterning IGZO for TFT devices, good device characteristics are necessary. Ideally the resist should not alter IGZO electrical properties including mobility, turn-on voltage, and subthreshold swing. Transfer characteristics were obtained to evaluate the performance of the final devices with IGZO channels patterned using EHDP. Electrical parameters were calculated using methods described in Chapter 2. Optical microscope images of the final HPA and SU8 patterned devices are shown in Figure 30a and b, respectively. The

channel for both devices is 200 μm long and ~ 50 nm thick. The channel width for the HPA patterned IGZO TFT is ~ 2 μm . The channel width for the SU8 patterned is ~ 4 μm . Transfer characteristics of an unpatterned device were also obtained to compare with EHDP patterned devices. These devices were processed with identical 50 nm thick IGZO channels, but without patterning using etch resists.

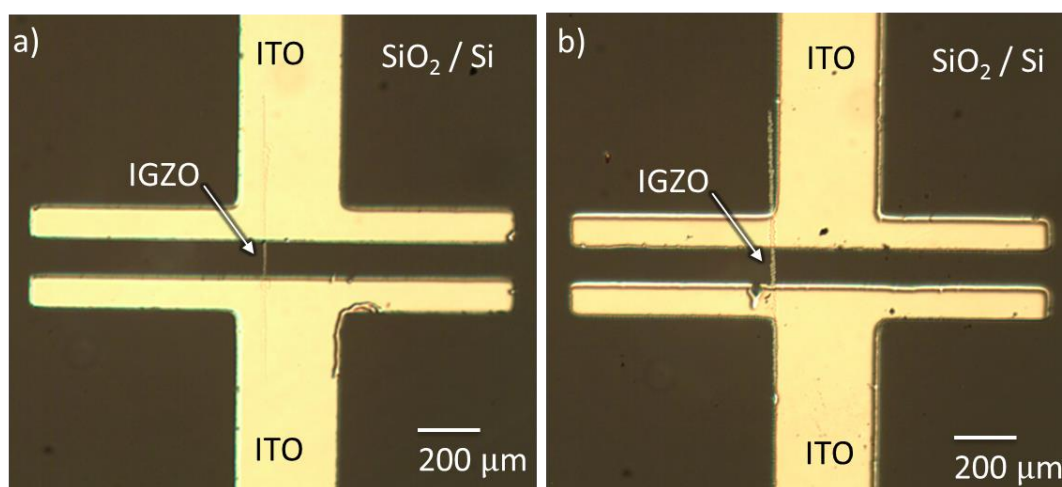


Figure 29. a) HPA patterned IGZO TFT with channel width ~ 2 μm . b) SU8 patterned IGZO TFT. Source and drain is Al and the gate dielectric is SiO₂. IGZO channels are 100 μm long and 50 nm thick.

The channel width and length of the unpatterned devices was 1000 μm and 100 μm , respectively. The transfer curve for an HPA patterned device is shown in Figure 31a and the average mobility is plotted in Figure 31b. The devices fabricated using the HPA ink had a turn-on voltage of ~ 9.7 V and hysteresis of ~ 0.38 V. The overall average mobility was found to be ~ 11.5 $\text{cm}^2/\text{V s}$. The $I_{\text{on}}/I_{\text{off}}$ ratio was found to be $\sim 7.3 \times 10^3$. The rather low $I_{\text{on}}/I_{\text{off}}$ ratio is due to the high I_{off} current $\sim 6 \times 10^{-9}$ A, compared to bulk film IGZO TFTs which had an off current less than 10^{-11} A. The SS of the IGZO channel was ~ 1.3 V/decade indicating a high number of trap states in the IGZO. Using the obtained SS and

Equation 6 the trap density (D_{sg}) was calculated to be $\sim 4.3 \times 10^{12} \text{ \# / cm}^2 \text{ eV}$. As the channel width is decreased the surface area to volume ratio increases and surface traps may dominate.

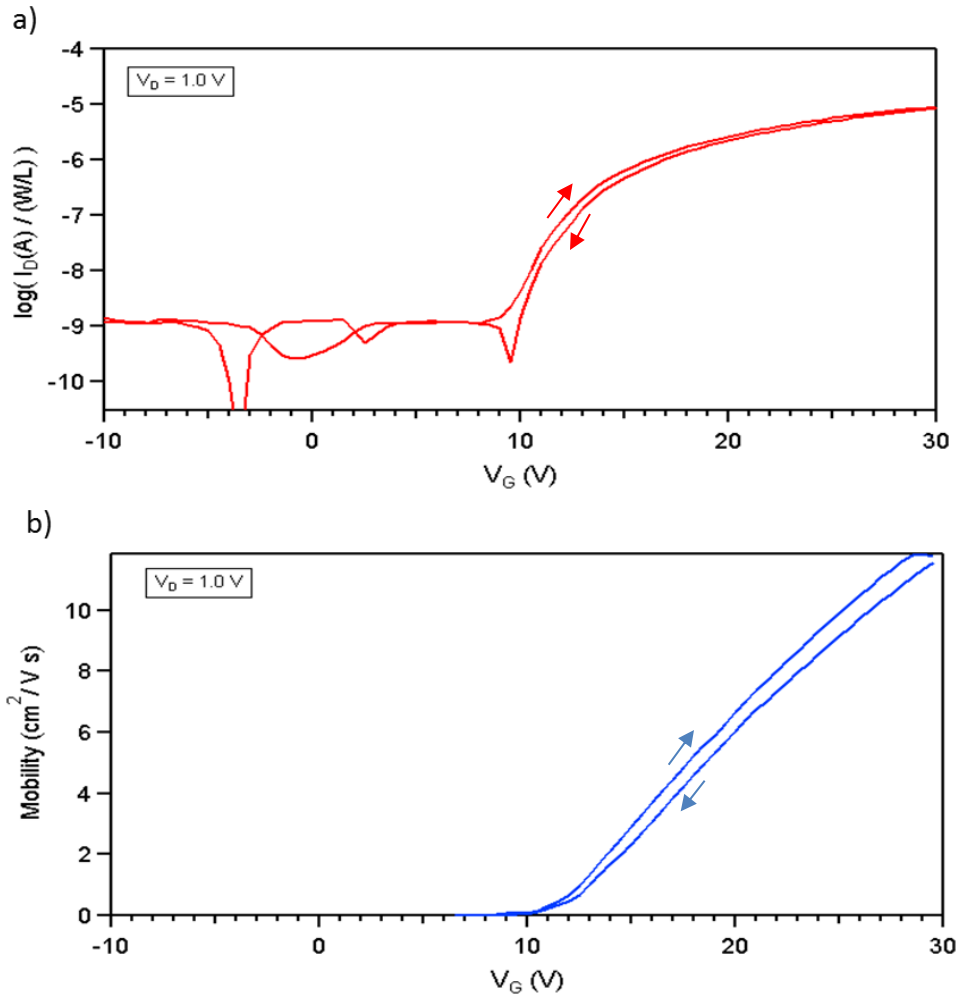


Figure 30. a) I-V transfer characteristic current output for IGZO TFTs patterned using HPA, normalized using L/W . b) Average mobility of HPA patterned TFTs. The arrows indicate the direction of the sweep.

The electrical performance of TFTs patterned using SU8 was evaluated using the same methods and conditions as the HPA patterned devices.

Figure 32a shows the transfer characteristics obtained from the SU8 patterned device. The V_{on} was ~ 7.9 V with a hysteresis of ~ 0.93 V between the up and down sweeps. The on/off ratio was $\sim 7.8 \times 10^4$ with a SS of ~ 2.1 V/decade. The IGZO channel mobility shown in Figure 32b monotonically increases as a function of V_g with an average mobility of ~ 8.5 $\text{cm}^2 / \text{V s}$.

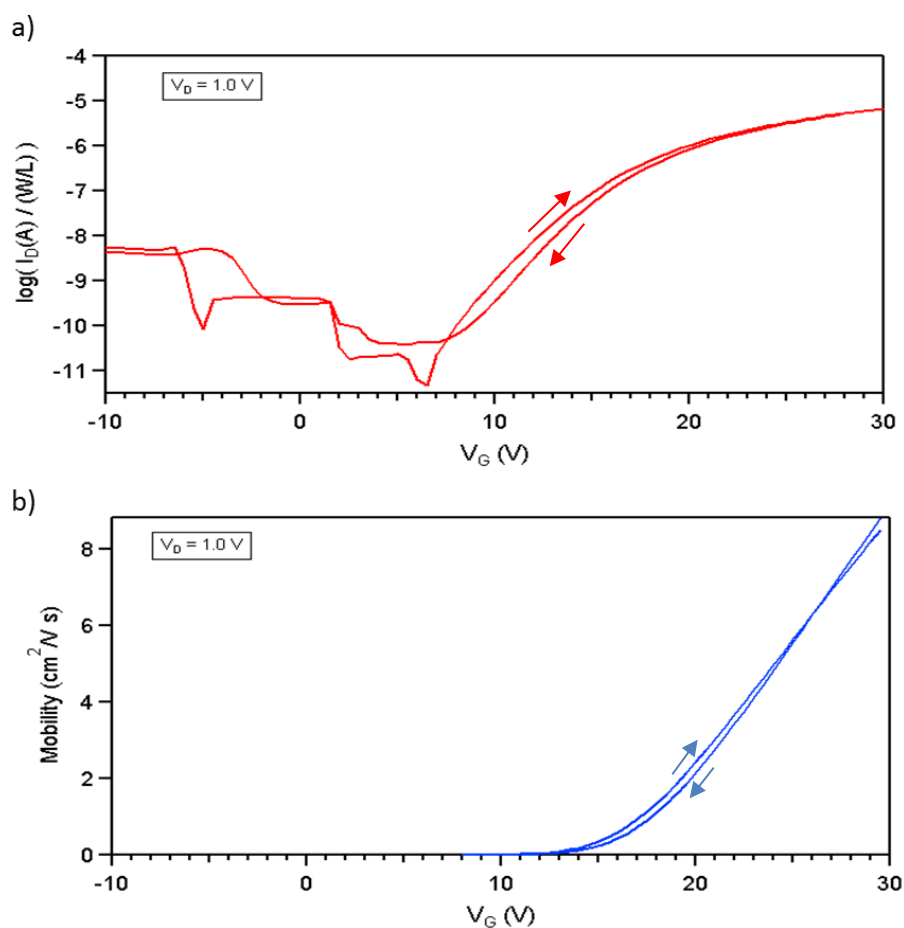


Figure 31. a) I-V transfer characteristics of IGZO TFT patterned using SU8, normalized using L/W . b) Average mobility of SU8 patterned TFTs. The arrows indicate the direction of the sweep.

Transfer characteristics were also obtained for a device without EHDP patterning for comparison. Table 5 summarizes the TFT electrical parameters for IGZO TFTs patterned

using EHDP and as deposited. The V_{on} of the unpatterned device was ~ 4.3 V with 1.1 V hysteresis, an average mobility of $7.1 \text{ cm}^2 / \text{V s}$, and SS ~ 0.38 V/decade.

Table 5. Summary of TFT electrical parameters for IGZO channels patterned using EHDP and unpatterned

	Von (V)	Hysteresis (V)	Mobility ($\text{cm}^2/\text{V s}$)	Sub Thres. Swing (V/dec)	On/off Ratio
SU8 Patterned	7.9	0.94	8.5	2.10	1.9E+04
HPA Patterned	9.7	0.39	10.5	1.26	7.3E+03
Unpatterned	4.3	1.06	7.1	0.38	6.4E+06

The on/off current ratio was lower for both the devices patterned using EHDP inks. All devices had similar I_{on} currents $\sim 10^{-6}$ A. However the off state current for the unpatterned device is 2 orders of magnitude lower. This is due to the higher width where current is controlled by W/L.

The unpatterned device showed the lowest V_{on} with the HPA patterned device exhibiting the largest V_{on} . The location of V_{on} is strongly related to the absolute number of carriers in the IGZO channel where increasing the number of carriers decreases V_{on} [35], [122]. One possible explanation for increases in V_{on} for the EHDP patterned devices is the lower number of free carriers creating. V_{on} shifted more positively for IGZO devices with decreased channel widths when stressed [123]. The shift was attributed to the trapping of holes at the channel/electrode interface. O_2 and H_2O absorbed to the IGZO surface is also known to effect IGZO TFT performance by acting as electron donor or acceptors, respectfully [38], [65], [97]. For the narrow IGZO channels, absorbed molecules may influence V_{on} due to the higher surface area to volume.

The SS showed large differences between the patterned and unpatterned devices. The SS is determined by the trap state density in the channel. The films patterned using EHDP exhibit lower SS indicating a higher trap density. The total trap density is a combination of trap states in the bulk film and trap states at the channel interfaces. The ratio of surface area to volume increases significantly as the size of the channel is decreased, meaning that surface area becomes more significant as the volume is reduced. As the width of the channel is decreased the surface trap states become more important in the TFT performance. The bulk density trap states is expected be similar for all samples since all films were deposited using the same deposition and annealing conditions. The narrower channels resulted in a greater SS due to the increase in influences from surface trap states. XPS studies of various thicknesses of IGZO channels reveals that a majority of the surface traps are deep subgap states ~ 1.2 eV below the Fermi level, and just above the VBM [91]. Deep subgap states do not contribute to generating electron carriers but do act as recombination centers for holes and free electrons.

Edge effects are known to influence polysilicon TFT performance due to variations in electric field [124]. Sharp edges concentrate the electric field causing non-uniform fields along the channel. Local variations in the electric field from V_G causes regions of the channel to turn on non-uniformly, forming parasitic transistors within the channel [125]. Parasitic transistors create variations in conductance within the IGZO channel which degrades SS and shift V_{on} . Parasitic transistor behavior has been observed in IGZO TFTs as indicated by a hump in the subthreshold regime on the transfer characteristic curve

[125]. The EHDP patterned devices in Figure 30 exhibit high edge roughness. High edge roughness suggests that the channel edges of the EHDP patterned devices may have non-uniform thicknesses and sharp features. The combination of sharp features and variations in edge thickness result in different regions of the IGZO TFT to turn on at lower V_{on} , resulting in larger SS.

Overall EHDP has been demonstrated as a means to deposit both commonly used photoresist, SU8, and SAMs for use as etch resists for micro patterning of IGZO TFTs. Optimized printing parameters and ink formulation enables EHDP patterning of devices with feature sizes of sub 10 μm . The use of EHDP surpasses the resolution limits of conventional thermal or piezoelectric printing techniques. The EHDP patterned devices showed significantly higher subthreshold swings compared with the unpatterned device. These differences are attributed to the physical dimensions of the devices and not to the use of EHDP.

Chapter 5: Future Directions

Further Studies on ODP A Applied to the Back Channel

It has been found that the application of ODP A to the IGZO TFT back channel decreases V_{on} by at least 1 V for channel thicknesses 10-50nm. The device hysteresis is similarly decreased with the use of ODP A, while the mobility, SS, and on/off ratio are minimally impacted. For sensing purposes the gate needs to be able to control the channel conductivity while still being sensitive to the back channel chemistry. To further understand how ODP A influences the channel conductivity, thicker channels should be investigated. It has been estimated that V_G can fully control the channel up to ~40 nm for IGZO [96]. For IGZO channel thicknesses greater than 40 nm, charge shielding from carriers diminishes the gate's effective control over the surface region of the channel. For our studies, the 50 nm devices are still impacted by ODP A absorbed on the surface. However, we did not determine at what IGZO channel thickness that the back channel surface becomes shielded by charge in the bulk IGZO, or if shielding can block the effects of ODP A at all. Repeating these I-V studies and including 100, 150, and 200 nm thick IGZO channels could help determine the maximum thickness that can be used before charge shielding becomes a dominant factor in the device performance. For sensing purposes, this is important for understanding and optimizing the channel thickness for the highest sensitivity while retaining good reliability. The thinnest IGZO channel is likely to have the highest sensitivity to the environment exposed to the back channel. Thin channels (10-20 nm) may be more sensitive to the back channel chemistry.

Knowledge on how channel thickness effects molecular detection sensitivity will allow for design tradeoffs to be made between processing capabilities and device sensitivity.

Examining a wider range of thicknesses allows for estimating the bulk and surface trap densities. According to Equation 7, the total trap density should linearly increase as thicknesses increases. A linear fit can be used to determine the bulk and interface trap densities. The differentiation of bulk and surface traps allows for understanding how effective ODPA is at passivating the back channel. There can be many reasons for the observe decrease in V_{on} and hysteresis for devices with ODPA. The decrease in V_{on} can be attributed to an increase in carrier concentration or band bending at the back channel interface. I-V measurements alone cannot determine the carrier concentration.

Experiments utilizing Hall effect measurements can be used for determining the carrier mobility and free carrier concentration, as indicated by Equation 3 [85]. The difficulty with Hall effect measurements for IGZO is that the carrier concentration is low at room temperature. The Hall effect model for assumes Boltzmann transport theory and Arrhenius behavior of thermally activated carriers, where conductivity follows linear relationship with T^{-1} [27]. Since IGZO does not follow Arrhenius behavior of thermally activated carriers at low temperatures, Alder's percolation theory must be applied to accurately model the thermal behavior of carriers [27]. The percolation model uses a distribution of potential energy barriers resulting in linear conductivity when plotted against $T^{-1/4}$ [87]. The percolation model adds further complexity to the analysis but can accurately calculate intrinsic mobility and carrier concentration [27], [87]. An alternative

to Hall effect measurements for determining the carrier concentration is capacitance-voltage (C-V) measurements [126]. The use of C-V measurements can provide information on trap densities, while I-V measurements provide mobility estimates. However, the TFT structure required for C-V measurements requires the deposition of an electrode over the backchannel for measuring capacitance between the channel and gate. The electrode covers the back channel preventing it from exposure to the atmospheric environment. The influence of SAMs on carrier concentration can be studied through the use Hall effect and I-V measurements.

ODPA passivation can prevent from absorption of atmospheric molecules on the back channel which can also contribute to V_{on} shifts in and hysteresis. Since water or oxygen absorbed to the back channel of IGZO TFTs is known to act as electron donors or acceptors, respectfully, experiments can be constructed to help determine if reduction in hysteresis and V_{on} shifts are due to blocking absorption of atmospheric species [97]. I-V and Hall effect measurements can be made on devices with and without a SAM, exposed to controlled concentrations of water and oxygen. These experiments can provide information on how effective ODPA is at passivating the IGZO surface. Understanding how SAMs effect the back channel is important for developing functionalized IGZO TFTs as sensors. Similar experiments have demonstrated that SAMs are capable of effectively blocking water and oxygen from absorbing on surfaces [127], [128]. Molecules such as oxygen and water may interfere with the stability and reproducibility of measurements that are crucial for sensors. Sensors must be able to selectively detect

specific molecules while screening out interferent molecules. SAMs are advantageous for TFT sensing because they can both selectively functionalize and passivate the back channel. Therefore valuable information can be obtained by experiments that clarify whether the shifts in V_{on} and hysteresis are due to passivation of the IGZO surface or due to the bonding of ODPA to IGZO. Hall effect measurements can be combined to get further information on how SAMs can alter defect trap states.

Further Studies for Electrohydrodynamic Ink Jet Printed IGZO TFTs

The primary focus of Chapter 4 was to demonstrate sub-10 micron features by direct patterning using EHDP. The subthreshold swing and V_{on} were significantly different for devices patterned using EHDP compared to unpatterned devices. Variations in edge roughness and edge thickness likely cause parasitic regions that degrade device performance. Further optimization of ink wetting the IGZO surface could improve the distribution of droplet placement. Improved droplet uniformity should decrease edge roughness and variations in channel width. Investigating different solvents or combinations of solvents to control the solvent evaporation can enhance the coalescing of droplets. Alkyl phosphonic acid SAMs are soluble in a wide range of organic solvents such as ethanol, isopropanol, methanol, tetrahydrofuran, and dimethyl sulfoxide [129], [130]. Mixtures of these solvents can be studied to obtain optimal ink properties such as viscosity, evaporation rate, and contact angle. Controlling the ink viscosity allows for a wider range of printing parameters. Managing the evaporation rate can greatly increase

the ink's ability to form coalescing droplets and decrease line edge roughness. Control over the wetting of the printing surface is crucial for obtaining uniform droplet placement. The contact angle needs to be carefully considered when attempting to place droplets with uniform spreading. Examining mixtures of various solvents enables all these properties to be evaluated for optimizing printing conditions.

The versatility of EHDP enables a wide range of TFT fabrication studies using EHDP. Both the SU8 ink and HPA ink can be used for fabrication depending on the process requirements. SU8 ink forms a thicker line and can be used with used etchants commonly used in photolithography. This extends the potential use of SU8 inks to patterning other materials. The HPA ink can achieve higher resolution, however it has only been evaluated for etching with dilute HCl. Both inks can be used for the appropriate processing needs. EHDP has been demonstrated to print feature widths down to 200nm [50], and should allow studies on EHDP patterned channel widths to be performed over a broad range. For example, features wider than a single printed line can be obtained by rastering overlapping printed lines. The channel width can be varied by rastering lines of etch resist. Because it is suspected that the channel edge conditions decreased the printed device's performance, further studies varying the printed channel width are required to better evaluate EHDP for device fabrication. It would be expected that the edge effects will become less prominent as the channel width increases. Direct comparison of channels with the same width, as deposited and patterned using EHDP, would give a better evaluation of EHDP for patterning devices. EHDP allows for varying the

dimensions of micro scale devices without the need for designing multiple photomasks. This allows for easier fabrication and testing of various device layouts. Studying the effects of channel width is relevant to TFT sensors because the channel is used as the sensing region. Experiments for determining the best channel size can easily be implemented using EHDP. By printing various channel widths the device sensitivity can be evaluated as a function of channel width. It could be expected that long narrow channels reduce the parallel pathways for carriers to traverse from source to drain. The smaller channel surface area, and increased surface area to volume ratio, can increase sensitivity to lower concentrations of molecules. EHDP can be used to rapidly evaluate this hypothesis. The flexibility of digital patterning makes EHDP a good tool for quickly developing test structures. Further development of EHDP can enable for rapid fabrication of prototype or research devices with complex structures.

Works Cited

- [1] J. Wang, "Electrochemical Glucose Biosensors," *Chem. Rev.*, vol. 108, no. 2, pp. 814–825, Feb. 2008.
- [2] S. P. Nichols, A. Koh, W. L. Storm, J. H. Shin, and M. H. Schoenfisch, "Biocompatible Materials for Continuous Glucose Monitoring Devices," *Chem. Rev.*, vol. 113, no. 4, pp. 2528–2549, Apr. 2013.
- [3] H.-W. Zan, C.-H. Li, C.-C. Yeh, M.-Z. Dai, H.-F. Meng, and C.-C. Tsai, "Room-temperature-operated sensitive hybrid gas sensor based on amorphous indium gallium zinc oxide thin-film transistors," *Appl. Phys. Lett.*, vol. 98, no. 25, p. 253503, 2011.
- [4] J. Jung, S. J. Kim, D. H. Yoon, B. Kim, S. H. Park, and H. J. Kim, "Electrical Responses of Artificial DNA Nanostructures on Solution-Processed In-Ga-Zn-O Thin-Film Transistors with Multistacked Active Layers," *ACS Appl. Mater. Interfaces*, vol. 5, no. 1, pp. 98–102, Jan. 2013.
- [5] J.-Y. Kwon, D.-J. Lee, and K.-B. Kim, "Review Paper: Transparent Amorphous Oxide Semiconductor Thin Film Transistor," *Electron. Mater. Lett.*, vol. 7, no. 1, pp. 1–11, 2011.
- [6] P.-C. Wang, L.-H. Liu, D. Alemu Mengistie, K.-H. Li, B.-J. Wen, T.-S. Liu, and C.-W. Chu, "Transparent electrodes based on conducting polymers for display applications," *Displays*, vol. 34, no. 4, pp. 301–314, Oct. 2013.
- [7] J.-S. Park, T.-W. Kim, D. Stryakhilev, J.-S. Lee, S.-G. An, Y.-S. Pyo, D.-B. Lee, Y. G. Mo, D.-U. Jin, and H. K. Chung, "Flexible full color organic light-emitting diode display on polyimide plastic substrate driven by amorphous indium gallium zinc oxide thin-film transistors," *Appl. Phys. Lett.*, vol. 95, no. 1, p. 13503, 2009.
- [8] C.-Y. Lo, O.-H. Huttunen, J. Hiitola-Keinanen, J. Petaja, H. Fujita, and H. Toshiyoshi, "MEMS-Controlled Paper-Like Transmissive Flexible Display," *J. Microelectromechanical Syst.*, vol. 19, no. 2, pp. 410–418, Apr. 2010.
- [9] K. Nomura, A. Takagi, T. Kamiya, H. Ohta, M. Hirano, and H. Hosono, "Amorphous oxide semiconductors for high-performance flexible thin-film transistors," *Jpn. J. Appl. Phys.*, vol. 45, no. 5S, p. 4303, 2006.
- [10] H. Gleskova, S. Wagner, and Z. Suo, "Failure resistance of amorphous silicon transistors under extreme in-plane strain," *Appl. Phys. Lett.*, vol. 75, no. 19, p. 3011, 1999.
- [11] Y. Leterrier, L. Médico, F. Demarco, J.-A. E. Månson, U. Betz, M. F. Escolà, M. Kharrazi Olsson, and F. Atamny, "Mechanical integrity of transparent conductive oxide films for flexible polymer-based displays," *Thin Solid Films*, vol. 460, no. 1–2, pp. 156–166, Jul. 2004.
- [12] Z. Chen, B. Cotterell, W. Wang, and S.-J. Chua, "A Mechanical Assessment of Flexible Optoelectronic Devices," *Thin Solid Films*, vol. 394, pp. 201–206, 2001.
- [13] S. Kasap and P. Capper, *Springer Handbook of Electronic and Photonic Materials*. Springer Science & Business Media, 2006.
- [14] M. Ohring, *Materials Science of Thin Films*, 2nd ed. San Diego, CA, USA: Academic Press, 2002.
- [15] T. P. Brody, "The thin film transistor - A late flowering bloom," *IEEE Trans.*

Electron Devices, vol. 31, no. 11, pp. 1614–1628, Nov. 1984.

[16] S. Wolf and R. Tauber, *Silicon Processing for the VLSI Era*, vol. 1. Sunset Beach, California: Lattice Press, 1986.

[17] G. Darlinski, U. Böttger, R. Waser, H. Klauk, M. Halik, U. Zschieschang, G. Schmid, and C. Dehm, “Mechanical force sensors using organic thin-film transistors,” *J. Appl. Phys.*, vol. 97, no. 9, p. 93708, 2005.

[18] K. S. Chang, C. C. Chen, J. T. Sheu, and Y.-K. Li, “Detection of an uncharged steroid with a silicon nanowire field-effect transistor,” *Sens. Actuators B Chem.*, vol. 138, no. 1, pp. 148–153, Apr. 2009.

[19] X.-L. Luo, J.-J. Xu, W. Zhao, and H.-Y. Chen, “Glucose biosensor based on ENFET doped with SiO₂ nanoparticles,” *Sens. Actuators B Chem.*, vol. 97, no. 2–3, pp. 249–255, Feb. 2004.

[20] X. Du, C. J. Durgan, D. J. Matthews, J. R. Motley, X. Tan, K. Pholsena, L. Árnadóttir, J. R. Castle, P. G. Jacobs, R. S. Cargill, and others, “Fabrication of a Flexible Amperometric Glucose Sensor Using Additive Processes,” *ECS J. Solid State Sci. Technol.*, vol. 4, no. 4, pp. P3069–P3074, 2015.

[21] C.-S. Lee, S. K. Kim, and M. Kim, “Ion-Sensitive Field-Effect Transistor for Biological Sensing,” *Sensors*, vol. 9, no. 9, pp. 7111–7131, Sep. 2009.

[22] X. Du, Y. Li, J. R. Motley, W. F. Stickle, and G. S. Herman, “Glucose Sensing Using Functionalized Amorphous In-Ga-Zn-O Field Effect Transistors,” *ACS Appl. Mater. Interfaces*, vol. 8, no. 12, pp. 7631–7637, Mar. 2016.

[23] W. J. Maeng, J. S. Park, H.-S. Kim, E. S. Kim, K. S. Son, T. S. Kim, M. Ryu, and S. Lee, “The Effect of Active-Layer Thickness and Back-Channel Conductivity on the Subthreshold Transfer Characteristics of Hf-In-Zn-O TFTs,” *IEEE Electron Device Lett.*, vol. 32, no. 8, pp. 1077–1079, Aug. 2011.

[24] S. Y. Lee, D. H. Kim, E. Chong, Y. W. Jeon, and D. H. Kim, “Effect of channel thickness on density of states in amorphous InGaZnO thin film transistor,” *Appl. Phys. Lett.*, vol. 98, no. 12, p. 122105, 2011.

[25] M. G. Yun, S. H. Kim, C. H. Ahn, S. W. Cho, and H. K. Cho, “Effects of channel thickness on electrical properties and stability of zinc tin oxide thin-film transistors,” *J. Phys. Appl. Phys.*, vol. 46, no. 47, p. 475106, Nov. 2013.

[26] T. Kamiya, K. Nomura, and H. Hosono, “Origins of High Mobility and Low Operation Voltage of Amorphous Oxide TFTs: Electronic Structure, Electron Transport, Defects and Doping,” *J. Disp. Technol.*, vol. 5, no. 7, pp. 273–288, Jul. 2009.

[27] T. Kamiya, K. Nomura, and H. Hosono, “Origin of definite Hall voltage and positive slope in mobility-donor density relation in disordered oxide semiconductors,” *Appl. Phys. Lett.*, vol. 96, no. 12, p. 122103, 2010.

[28] “LG Display says UHD OLED TV panel products in various sizes and designs in 2015,” *Flat Panel TV and Display World*, 27-May-2013. [Online]. Available: <http://flat-display-2.livedoor.biz/archives/28524794.html>. [Accessed: 14-Mar-2016].

[29] “Sharp Begins Production of World’s First LCD Panels Incorporating IGZO Oxide Semiconductors,” *Sharp-world.com*, 13-Apr-2012. [Online]. Available: <http://www.sharp-world.com/corporate/news/120413.html>. [Accessed: 14-Mar-2016].

[30] K. Nomura, T. Kamiya, H. Yanagi, E. Ikenaga, K. Yang, K. Kobayashi, M.

- Hirano, and H. Hosono, "Subgap states in transparent amorphous oxide semiconductor, In-Ga-Zn-O, observed by bulk sensitive x-ray photoelectron spectroscopy," *Appl. Phys. Lett.*, vol. 92, no. 20, p. 202117, 2008.
- [31] L. Je-hun, Y. Do-hyun, H. Sun-yung, Y. Kap-soo, H. Pil-soon, L. Soon Kwon, and K. Sang Soo, "42.2: World's Largest (15-inch) XGA AMLCD Panel Using IGZO Oxide TFT," *SID Symp. Dig. Tech. Pap.*, vol. 39, no. 1, pp. 625–628, 2008.
- [32] J. K. Jeong, J. H. Jeong, H. W. Yang, T. K. Ahn, M. Kim, K. S. Kim, B. S. Gu, H.-J. Chung, J.-S. Park, Y.-G. Mo, H. D. Kim, and H. K. Chung, "12.1-in. WXGA AMOLED display driven by InGaZnO thin-film transistors," *J. Soc. Inf. Disp.*, vol. 17, no. 2, p. 95, 2009.
- [33] L. Li, L. Fan, Y. Li, Z. Song, F. Ma, and C. Liu, "Effect of thermal annealing on the properties of transparent conductive In-Ga-Zn oxide thin films," *J. Vac. Sci. Technol. Vac. Surf. Films*, vol. 32, no. 2, p. 21506, Mar. 2014.
- [34] K. Nomura, T. Kamiya, H. Ohta, M. Hirano, and H. Hosono, "Defect passivation and homogenization of amorphous oxide thin-film transistor by wet O₂ annealing," *Appl. Phys. Lett.*, vol. 93, no. 19, p. 192107, 2008.
- [35] C. H. Woo, Y. Y. Kim, B. H. Kong, and H. K. Cho, "Effects of the thickness of the channel layer on the device performance of InGaZnO thin-film-transistors," *Surf. Coat. Technol.*, vol. 205, pp. S168–S171, Dec. 2010.
- [36] X. Ding, J. Zhang, J. Li, H. Zhang, W. Shi, X. Jiang, and Z. Zhang, "Influence of the InGaZnO channel layer thickness on the performance of thin film transistors," *Superlattices Microstruct.*, vol. 63, pp. 70–78, Nov. 2013.
- [37] H. Q. Chiang, B. R. McFarlane, D. Hong, R. E. Presley, and J. F. Wager, "Processing effects on the stability of amorphous indium gallium zinc oxide thin-film transistors," *J. Non-Cryst. Solids*, vol. 354, no. 19–25, pp. 2826–2830, May 2008.
- [38] J.-S. Park, J. K. Jeong, H.-J. Chung, Y.-G. Mo, and H. D. Kim, "Electronic transport properties of amorphous indium-gallium-zinc oxide semiconductor upon exposure to water," *Appl. Phys. Lett.*, vol. 92, no. 7, p. 72104, 2008.
- [39] S.-Y. Sung, J. H. Choi, U. B. Han, K. C. Lee, J.-H. Lee, J.-J. Kim, W. Lim, S. J. Pearton, D. P. Norton, and Y.-W. Heo, "Effects of ambient atmosphere on the transfer characteristics and gate-bias stress stability of amorphous indium-gallium-zinc oxide thin-film transistors," *Appl. Phys. Lett.*, vol. 96, no. 10, p. 102107, 2010.
- [40] H.-S. Seo, J.-U. Bae, D.-H. Kim, Y. Park, C.-D. Kim, I. B. Kang, I.-J. Chung, J.-H. Choi, and J.-M. Myoung, "Reliable Bottom Gate Amorphous Indium-Gallium-Zinc Oxide Thin-Film Transistors with TiO_x Passivation Layer," *Electrochem. Solid-State Lett.*, vol. 12, no. 9, p. H348, 2009.
- [41] T. T. T. Nguyen, B. Aventurier, T. Terlier, J.-P. Barnes, and F. Templier, "Impact of Passivation Conditions on Characteristics of Bottom-Gate IGZO Thin-Film Transistors," *J. Disp. Technol.*, vol. 11, no. 6, pp. 554–558, Jun. 2015.
- [42] A. Ulman, "Formation and structure of self-assembled monolayers," *Chem. Rev.*, vol. 96, no. 4, pp. 1533–1554, 1996.
- [43] J. C. Love, L. A. Estroff, J. K. Kriebel, R. G. Nuzzo, and G. M. Whitesides, "Self-Assembled Monolayers of Thiolates on Metals as a Form of Nanotechnology," *Chem. Rev.*, vol. 105, no. 4, pp. 1103–1170, Apr. 2005.

- [44] P. J. Hotchkiss, M. Malicki, A. J. Giordano, N. R. Armstrong, and S. R. Marder, "Characterization of phosphonic acid binding to zinc oxide," *J. Mater. Chem.*, vol. 21, no. 9, p. 3107, 2011.
- [45] W. Gao, L. Dickinson, C. Grozinger, F. G. Morin, and L. Reven, "Self-assembled monolayers of alkylphosphonic acids on metal oxides," *Langmuir*, vol. 12, no. 26, pp. 6429–6435, 1996.
- [46] S.-H. Cho, Y.-U. Lee, J.-S. Lee, K.-M. Jo, D.-H. Kim, B.-S. Kim, and M.-K. Han, "The Effects of Self Assembled Monolayer (SAM) on the Back Back Interface of a-IGZO TFT," in *Meeting Abstracts*, 2011, pp. 1150–1150.
- [47] S. A. Paniagua, P. J. Hotchkiss, S. C. Jones, S. R. Marder, A. Mudalige, F. S. Marrikar, J. E. Pemberton, and N. R. Armstrong, "Phosphonic Acid Modification of Indium–Tin Oxide Electrodes: Combined XPS/UPS/Contact Angle Studies," *J. Phys. Chem. C*, vol. 112, no. 21, pp. 7809–7817, May 2008.
- [48] B. Derby, "Inkjet Printing of Functional and Structural Materials: Fluid Property Requirements, Feature Stability, and Resolution," *Annu. Rev. Mater. Res.*, vol. 40, no. 1, pp. 395–414, 2010.
- [49] G. Taylor, "Disintegration of Water Drops in an Electric Field," *Proc. R. Soc. Lond. Math. Phys. Eng. Sci.*, vol. 280, no. 1382, pp. 183–197, 1964.
- [50] B. H. Kim, M. S. Onses, J. B. Lim, S. Nam, N. Oh, H. Kim, K. J. Yu, J. W. Lee, J.-H. Kim, S.-K. Kang, C. H. Lee, J. Lee, J. H. Shin, N. H. Kim, C. Leal, M. Shim, and J. A. Rogers, "High-Resolution Patterns of Quantum Dots Formed by Electrohydrodynamic Jet Printing for Light-Emitting Diodes," *Nano Lett.*, vol. 15, no. 2, pp. 969–973, Feb. 2015.
- [51] J.-U. Park, M. Hardy, S. J. Kang, K. Barton, K. Adair, D. kishore Mukhopadhyay, C. Y. Lee, M. S. Strano, A. G. Alleyne, J. G. Georgiadis, P. M. Ferreira, and J. A. Rogers, "High-resolution electrohydrodynamic jet printing," *Nat. Mater.*, vol. 6, no. 10, pp. 782–789, Oct. 2007.
- [52] K. Shigeta, Y. He, E. Sutanto, S. Kang, A.-P. Le, R. G. Nuzzo, A. G. Alleyne, P. M. Ferreira, Y. Lu, and J. A. Rogers, "Functional Protein Microarrays by Electrohydrodynamic Jet Printing," *Anal. Chem.*, vol. 84, no. 22, pp. 10012–10018, Nov. 2012.
- [53] "Agilent 4155C Semiconductor Parameter Analyzer User's Guide." Agilent Technologies, 2008.
- [54] K. Nomura, T. Kamiya, Y. Kikuchi, M. Hirano, and H. Hosono, "Comprehensive studies on the stabilities of a-In-Ga-Zn-O based thin film transistor by constant current stress," *Thin Solid Films*, vol. 518, no. 11, pp. 3012–3016, Mar. 2010.
- [55] R. L. Hoffman, "ZnO-channel thin-film transistors: Channel mobility," *J. Appl. Phys.*, vol. 95, no. 10, p. 5813, 2004.
- [56] D. Hong, G. Yerubandi, H. Q. Chiang, M. C. Spiegelberg, and J. F. Wager, "Electrical Modeling of Thin-Film Transistors," *Crit. Rev. Solid State Mater. Sci.*, vol. 33, no. 2, pp. 101–132, May 2008.
- [57] F. Zhou, B.-S. Yeh, K. A. Archila, and J. F. Wager, "Mobility Assessment of Depletion-Mode Oxide Thin-Film Transistors Using the Comprehensive Depletion-Mode Model," *ECS J. Solid State Sci. Technol.*, vol. 3, no. 9, pp. Q3027–Q3031, Jul. 2014.

- [58] E. Fortunato, P. Barquinha, and R. Martins, "Oxide Semiconductor Thin-Film Transistors: A Review of Recent Advances," *Adv. Mater.*, vol. 24, no. 22, pp. 2945–2986, Jun. 2012.
- [59] S. Logothetidis, "Flexible organic electronic devices: Materials, process and applications," *Mater. Sci. Eng. B*, vol. 152, no. 1–3, pp. 96–104, Aug. 2008.
- [60] H.-H. Hsieh, H.-H. Lu, H.-C. Ting, C.-S. Chuang, C.-Y. Chen, and Y. Lin, "Development of IGZO TFTs and their applications to next-generation flat-panel displays," *J. Inf. Disp.*, vol. 11, no. 4, pp. 160–164, 2010.
- [61] J. S. Park, W.-J. Maeng, H.-S. Kim, and J.-S. Park, "Review of recent developments in amorphous oxide semiconductor thin-film transistor devices," *Thin Solid Films*, vol. 520, no. 6, pp. 1679–1693, Jan. 2012.
- [62] J.-C. Lin, B.-R. Huang, and Y.-K. Yang, "IGZO nanoparticle-modified silicon nanowires as extended-gate field-effect transistor pH sensors," *Sens. Actuators B Chem.*, vol. 184, pp. 27–32, Jul. 2013.
- [63] D. J. Yang, G. C. Whitfield, N. G. Cho, P.-S. Cho, I.-D. Kim, H. M. Saltsburg, and H. L. Tuller, "Amorphous InGaZnO₄ films: Gas sensor response and stability," *Sens. Actuators B Chem.*, vol. 171–172, pp. 1166–1171, Aug. 2012.
- [64] S.-J. Kim, S.-Y. Lee, Y.-W. Lee, W.-G. Lee, K.-S. Yoon, J.-Y. Kwon, and M.-K. Han, "Effect of Channel Layer Thickness on Characteristics and Stability of Amorphous Hafnium–Indium–Zinc Oxide Thin Film Transistors," *Jpn. J. Appl. Phys.*, vol. 50, no. 2, p. 24104, Feb. 2011.
- [65] D. Kang, H. Lim, C. Kim, I. Song, J. Park, Y. Park, and J. Chung, "Amorphous gallium indium zinc oxide thin film transistors: Sensitive to oxygen molecules," *Appl. Phys. Lett.*, vol. 90, no. 19, p. 192101, 2007.
- [66] C.-S. Fuh, P.-T. Liu, Y.-T. Chou, L.-F. Teng, and S. M. Sze, "Role of Oxygen in Amorphous In-Ga-Zn-O Thin Film Transistor for Ambient Stability," *ECS J. Solid State Sci. Technol.*, vol. 2, no. 1, pp. Q1–Q5, 2013.
- [67] C. G. Choi, S.-J. Seo, and B.-S. Bae, "Solution-Processed Indium-Zinc Oxide Transparent Thin-Film Transistors," *Electrochem. Solid-State Lett.*, vol. 11, no. 1, p. H7, 2008.
- [68] M. Stewart, R. S. Howell, L. Pires, and M. K. Hatalis, "Polysilicon TFT technology for active matrix OLED displays," *IEEE Trans. Electron Devices*, vol. 48, no. 5, pp. 845–851, May 2001.
- [69] S. Higashi, D. Abe, Y. Hiroshima, K. Miyashita, T. Kawamura, S. Inoue, and T. Shimoda, "High-quality SiO₂/Si interface formation and its application to fabrication of low-temperature-processed polycrystalline Si thin-film transistor," *Jpn. J. Appl. Phys.*, vol. 41, no. 6R, p. 3646, 2002.
- [70] J. Lewis, "Material challenge for flexible organic devices," *Mater. Today*, vol. 9, no. 4, pp. 38–45, 2006.
- [71] K. Nomura, H. Ohta, K. Takagi, M. Hirano, and H. Hosono, "Room-temperature fabrication of transparent flexible thin-film transistors using amorphous oxide semiconductors," *Laser Part. Beams*, vol. 432, no. 7016, pp. 488–492, 2004.
- [72] H. Yabuta, M. Sano, K. Abe, T. Aiba, T. Den, H. Kumomi, K. Nomura, T. Kamiya, and H. Hosono, "High-mobility thin-film transistor with amorphous InGaZnO₄

- channel fabricated by room temperature rf-magnetron sputtering,” *Appl. Phys. Lett.*, vol. 89, no. 11, p. 112123, 2006.
- [73] T. Aoi, N. Oka, Y. Sato, R. Hayashi, H. Kumomi, and Y. Shigesato, “DC sputter deposition of amorphous indium–gallium–zinc–oxide (a-IGZO) films with H₂O introduction,” *Thin Solid Films*, vol. 518, no. 11, pp. 3004–3007, Mar. 2010.
- [74] M. Kim, J. H. Jeong, H. J. Lee, T. K. Ahn, H. S. Shin, J.-S. Park, J. K. Jeong, Y.-G. Mo, and H. D. Kim, “High mobility bottom gate InGaZnO thin film transistors with SiO_x etch stopper,” *Appl. Phys. Lett.*, vol. 90, no. 21, p. 212114, 2007.
- [75] A. Hino, Y. Takanashi, H. Tao, S. Morita, M. Ochi, H. Goto, K. Hayashi, and T. Kugimiya, “Effects of thermal annealing on variations of electron traps in the channel region of amorphous In-Ga-Zn-O thin film transistor,” *J. Vac. Sci. Technol. B Microelectron. Nanometer Struct.*, vol. 32, no. 3, p. 31210, May 2014.
- [76] S. Oliver, “Display makers increase IGZO capacity as Apple ponders next-gen panels for ‘iPad Pro’ - report,” *AppleInsider*, 06-Apr-2015. [Online]. Available: <http://appleinsider.com/articles/15/04/06/display-makers-increase-igzo-capacity-as-apple-ponders-next-gen-panels-for-ipad-pro---report>. [Accessed: 19-Apr-2016].
- [77] K. Nomura, T. Kamiya, H. Ohta, K. Shimizu, M. Hirano, and H. Hosono, “Relationship between non-localized tail states and carrier transport in amorphous oxide semiconductor, In–Ga–Zn–O,” *Phys. Status Solidi A*, vol. 205, no. 8, pp. 1910–1914, Aug. 2008.
- [78] D. Alder, L. Flora, and S. Senturia, “Electrical Conductivity in Disordered Systems,” *Solid State Commun.*, vol. 12, no. 1, pp. 9–12, 1973.
- [79] T. Kamiya, K. Nomura, and H. Hosono, “Present status of amorphous In–Ga–Zn–O thin-film transistors,” *Sci. Technol. Adv. Mater.*, vol. 11, no. 4, p. 44305, Aug. 2010.
- [80] G. Li, B.-R. Yang, C. Liu, C.-Y. Lee, C.-Y. Tseng, C.-C. Lo, A. Lien, S. Deng, H.-P. D. Shieh, and N. Xu, “Positive gate bias instability alleviated by self-passivation effect in amorphous InGaZnO thin-film transistors,” *J. Phys. Appl. Phys.*, vol. 48, no. 47, p. 475107, Dec. 2015.
- [81] L.-Y. Su, H.-Y. Lin, H.-K. Lin, S.-L. Wang, L.-H. Peng, and J. Huang, “Characterizations of Amorphous IGZO Thin-Film Transistors With Low Subthreshold Swing,” *IEEE Electron Device Lett.*, vol. 32, no. 9, pp. 1245–1247, Sep. 2011.
- [82] Sangwon Lee, Sungwook Park, Sungchul Kim, Yongwoo Jeon, Kichan Jeon, Jun-Hyun Park, Jaechul Park, Ihun Song, Chang Jung Kim, Youngsoo Park, Dong Myong Kim, and Dae Hwan Kim, “Extraction of Subgap Density of States in Amorphous InGaZnO Thin-Film Transistors by Using Multifrequency Capacitance-Voltage Characteristics,” *IEEE Electron Device Lett.*, vol. 31, no. 3, pp. 231–233, Mar. 2010.
- [83] M. Kimura, T. Nakanishi, K. Nomura, T. Kamiya, and H. Hosono, “Trap densities in amorphous InGaZnO₄ thin film transistors,” *Appl. Phys. Lett.*, vol. 92, no. 13, p. 133512, 2008.
- [84] T. Kamiya, K. Nomura, M. Hirano, and H. Hosono, “Electronic structure of oxygen deficient amorphous oxide semiconductor a-InGaZnO_{4-x}: Optical analyses and first-principle calculations,” *Phys. Status Solidi C*, vol. 5, no. 9, pp. 3098–3100, Jul. 2008.
- [85] A. Takagi, K. Nomura, H. Ohta, H. Yanagi, T. Kamiya, M. Hirano, and H.

- Hosono, "Carrier transport and electronic structure in amorphous oxide semiconductor, a-InGaZnO₄," *Thin Solid Films*, vol. 486, no. 1–2, pp. 38–41, Aug. 2005.
- [86] K. Nomura, T. Kamiya, M. Hirano, and H. Hosono, "Origins of threshold voltage shifts in room-temperature deposited and annealed a-In–Ga–Zn–O thin-film transistors," *Appl. Phys. Lett.*, vol. 95, no. 1, p. 13502, 2009.
- [87] T. Kamiya, K. Nomura, and H. Hosono, "Electronic Structures Above Mobility Edges in Crystalline and Amorphous In-Ga-Zn-O: Percolation Conduction Examined by Analytical Model," *J. Disp. Technol.*, vol. 5, no. 12, pp. 462–467, Dec. 2009.
- [88] M. E. Lopes, H. L. Gomes, M. C. R. Medeiros, P. Barquinha, L. Pereira, E. Fortunato, R. Martins, and I. Ferreira, "Gate-bias stress in amorphous oxide semiconductors thin-film transistors," *Appl. Phys. Lett.*, vol. 95, no. 6, p. 63502, 2009.
- [89] M. Nakata, H. Tsuji, H. Sato, Y. Nakajima, Y. Fujisaki, T. Takei, T. Yamamoto, and H. Fujikake, "Influence of Oxide Semiconductor Thickness on Thin-Film Transistor Characteristics," *Jpn. J. Appl. Phys.*, vol. 52, no. 3S, p. 03BB04, Mar. 2013.
- [90] Y. Li, Y. L. Pei, R. Q. Hu, Z. M. Chen, Y. Zhao, Z. Shen, B. F. Fan, J. Liang, and G. Wang, "Effect of channel thickness on electrical performance of amorphous IGZO thin-film transistor with atomic layer deposited alumina oxide dielectric," *Curr. Appl. Phys.*, vol. 14, no. 7, pp. 941–945, Jul. 2014.
- [91] K. Nomura, T. Kamiya, E. Ikenaga, H. Yanagi, K. Kobayashi, and H. Hosono, "Depth analysis of subgap electronic states in amorphous oxide semiconductor, a-In-Ga-Zn-O, studied by hard x-ray photoelectron spectroscopy," *J. Appl. Phys.*, vol. 109, no. 7, p. 73726, 2011.
- [92] B. Zhang, H. Li, X. Zhang, Y. Luo, Q. Wang, and A. Song, "Performance regeneration of InGaZnO transistors with ultra-thin channels," *Appl. Phys. Lett.*, vol. 106, no. 9, p. 93506, Mar. 2015.
- [93] X. Du, B. T. Flynn, J. R. Motley, W. F. Stickle, H. Bluhm, and G. S. Herman, "Role of Self-Assembled Monolayers on Improved Electrical Stability of Amorphous In-Ga-Zn-O Thin-Film Transistors," *ECS J. Solid State Sci. Technol.*, vol. 3, no. 9, pp. Q3045–Q3049, 2014.
- [94] P. Barquinha, A. Pimentel, A. Marques, L. Pereira, R. Martins, and E. Fortunato, "Influence of the semiconductor thickness on the electrical properties of transparent TFTs based on indium zinc oxide," *J. Non-Cryst. Solids*, vol. 352, no. 9–20, pp. 1749–1752, Jun. 2006.
- [95] A. H. Chen, H. T. Cao, H. Z. Zhang, L. Y. Liang, Z. M. Liu, Z. Yu, and Q. Wan, "Influence of the channel layer thickness on electrical properties of indium zinc oxide thin-film transistor," *Microelectron. Eng.*, vol. 87, no. 10, pp. 2019–2023, Oct. 2010.
- [96] C. Hsu, H. Chen, and S. Wang, "Effects of Localized Back-Surface Defects on Bulk and Front-Channel Conduction of Amorphous InGaZnO TFTs," *IEEE Trans. Electron Devices*, vol. 63, no. 1, pp. 369–376, Jan. 2016.
- [97] J. K. Jeong, H. Won Yang, J. H. Jeong, Y.-G. Mo, and H. D. Kim, "Origin of threshold voltage instability in indium-gallium-zinc oxide thin film transistors," *Appl. Phys. Lett.*, vol. 93, no. 12, p. 123508, 2008.
- [98] D. Kong, H.-K. Jung, Y. Kim, M. Bae, Y. W. Jeon, S. Kim, D. M. Kim, and D. H. Kim, "The Effect of the Active Layer Thickness on the Negative Bias Stress-Induced

- Instability in Amorphous InGaZnO Thin-Film Transistors,” *IEEE Electron Device Lett.*, vol. 32, no. 10, pp. 1388–1390, Oct. 2011.
- [99] Y. J. Kwack and W. S. Choi, “Electrohydrodynamic Jet Printed Indium Zinc Oxide Thin-Film Transistors,” *J. Disp. Technol.*, vol. 12, no. 1, pp. 3–7, Jan. 2016.
- [100] A. Khan, K. Rahman, M.-T. Hyun, D.-S. Kim, and K.-H. Choi, “Multi-nozzle electrohydrodynamic inkjet printing of silver colloidal solution for the fabrication of electrically functional microstructures,” *Appl. Phys. A*, vol. 104, no. 4, pp. 1113–1120, Sep. 2011.
- [101] K. Rahman, A. Khan, N. M. Muhammad, J. Jo, and K.-H. Choi, “Fine-resolution patterning of copper nanoparticles through electrohydrodynamic jet printing,” *J. Micromechanics Microengineering*, vol. 22, no. 6, p. 65012, Jun. 2012.
- [102] M. W. Lee, S. An, N. Y. Kim, J. H. Seo, J.-Y. Huh, H. Y. Kim, and S. S. Yoon, “Effects of pulsing frequency on characteristics of electrohydrodynamic inkjet using micro-Al and nano-Ag particles,” *Exp. Therm. Fluid Sci.*, vol. 46, pp. 103–110, Apr. 2013.
- [103] E. Elele, Y. Shen, R. Susarla, B. Khusid, G. Keyvan, and B. Michniak-Kohn, “Electrodeless electrohydrodynamic drop-on-demand encapsulation of drugs into porous polymer films for fabrication of personalized dosage units,” *J. Pharm. Sci.*, vol. 101, no. 7, pp. 2523–2533, Jul. 2012.
- [104] C. Wei, H. Qin, N. A. Ramírez-Iglesias, C.-P. Chiu, Y. Lee, and J. Dong, “High-resolution ac-pulse modulated electrohydrodynamic jet printing on highly insulating substrates,” *J. Micromechanics Microengineering*, vol. 24, no. 4, p. 45010, Apr. 2014.
- [105] K.-H. Kim and J.-K. Song, “Technical evolution of liquid crystal displays,” *NPG Asia Mater.*, vol. 1, no. 1, pp. 29–36, Oct. 2009.
- [106] “MacBook Pro with Retina display - Technical Specifications - Apple.” [Online]. Available: <http://www.apple.com/macbook-pro/specs-retina/>. [Accessed: 11-Apr-2016].
- [107] “Samsung Galaxy S4 mini preview: First look,” *GSMarena.com*. [Online]. Available: http://www.gsmarena.com/samsung_galaxy_s4_mini-review-932.php. [Accessed: 08-May-2016].
- [108] A. Lee, H. Jin, H.-W. Dang, K.-H. Choi, and K. H. Ahn, “Optimization of Experimental Parameters To Determine the Jetting Regimes in Electrohydrodynamic Printing,” *Langmuir*, vol. 29, no. 44, pp. 13630–13639, Nov. 2013.
- [109] A. Jaworek and A. Krupa, “Classification of the modes of EHD spraying,” *J. Aerosol Sci.*, vol. 30, no. 7, pp. 873–893, 1999.
- [110] M. W. Lee, D. K. Kang, N. Y. Kim, H. Y. Kim, S. C. James, and S. S. Yoon, “A study of ejection modes for pulsed-DC electrohydrodynamic inkjet printing,” *J. Aerosol Sci.*, vol. 46, pp. 1–6, Apr. 2012.
- [111] G. D. Martin, S. D. Hoath, and I. M. Hutchings, “Inkjet printing - the physics of manipulating liquid jets and drops,” *J. Phys. Conf. Ser.*, vol. 105, p. 12001, Mar. 2008.
- [112] K. Barton, S. Mishra, A. Shorter, A. Alleyne, P. Ferreira, and J. Rogers, “A Desktop Electrohydrodynamic Jet Printing System,” *Mechatronics*, vol. 20, pp. 611–616, 2010.
- [113] E. Sutanto, K. Shigeta, Y. K. Kim, P. G. Graf, D. J. Hoelzle, K. L. Barton, A. G. Alleyne, P. M. Ferreira, and J. A. Rogers, “A multimaterial electrohydrodynamic jet (E-

- jet) printing system,” *J. Micromechanics Microengineering*, vol. 22, no. 4, p. 45008, Apr. 2012.
- [114] C.-H. Chen, D. A. Saville, and I. A. Aksay, “Scaling laws for pulsed electrohydrodynamic drop formation,” *Appl. Phys. Lett.*, vol. 89, no. 12, p. 124103, 2006.
- [115] M. W. Lee, D. K. Kang, N. Y. Kim, H. Y. Kim, S. C. James, and S. S. Yoon, “A study of ejection modes for pulsed-DC electrohydrodynamic inkjet printing,” *J. Aerosol Sci.*, vol. 46, pp. 1–6, Apr. 2012.
- [116] “Nano (TM) SU-8 Negative Tone Photoresist Formulations 50-100.” Micro Chem, 2002.
- [117] P. J. Hotchkiss, S. C. Jones, S. A. Paniagua, A. Sharma, B. Kippelen, N. R. Armstrong, and S. R. Marder, “The Modification of Indium Tin Oxide with Phosphonic Acids: Mechanism of Binding, Tuning of Surface Properties, and Potential for Use in Organic Electronic Applications,” *Acc. Chem. Res.*, vol. 45, no. 3, pp. 337–346, Mar. 2012.
- [118] X. Du, R. T. Frederick, Y. Li, Z. Zhou, W. F. Stickle, and G. S. Herman, “Amorphous In-Ga-Zn-O thin-film transistors fabricated by microcontact printing,” *J. Vac. Sci. Technol. B Nanotechnol. Microelectron. Mater. Process. Meas. Phenom.*, vol. 33, no. 5, p. 52208, Sep. 2015.
- [119] O. A. Basaran, H. Gao, and P. P. Bhat, “Nonstandard Inkjets,” *Annu. Rev. Fluid Mech.*, vol. 45, no. 1, pp. 85–113, Jan. 2013.
- [120] J. Kim, H. Oh, and S. S. Kim, “Electrohydrodynamic drop-on-demand patterning in pulsed cone-jet mode at various frequencies,” *J. Aerosol Sci.*, vol. 39, no. 9, pp. 819–825, Sep. 2008.
- [121] “SU-8 2000 Series Resists; MSDS No. 11014,” MicroChem Corp., Newton, Ma, MSDS 11014.
- [122] J.-S. Park, J. K. Jeong, Y.-G. Mo, H. D. Kim, and C.-J. Kim, “Control of threshold voltage in ZnO-based oxide thin film transistors,” *Appl. Phys. Lett.*, vol. 93, no. 3, p. 33513, 2008.
- [123] S.-H. Choi and M.-K. Han, “Effect of channel widths on negative shift of threshold voltage, including stress-induced hump phenomenon in InGaZnO thin-film transistors under high-gate and drain bias stress,” *Appl. Phys. Lett.*, vol. 100, no. 4, p. 43503, 2012.
- [124] A. Valletta, P. Gaucchi, L. Mariucci, G. Fortunato, and F. Templier, “‘Hump’ characteristics and edge effects in polysilicon thin film transistors,” *J. Appl. Phys.*, vol. 104, no. 12, p. 124511, 2008.
- [125] M. Mativenga, M. Seok, and J. Jang, “Gate bias-stress induced hump-effect in transfer characteristics of amorphous-indium-galium-zinc-oxide thin-film transistors with various channel widths,” *Appl. Phys. Lett.*, vol. 99, no. 12, p. 122107, 2011.
- [126] M. Kimura, T. Kamiya, T. Nakanishi, K. Nomura, and H. Hosono, “Intrinsic carrier mobility in amorphous In–Ga–Zn–O thin-film transistors determined by combined field-effect technique,” *Appl. Phys. Lett.*, vol. 96, no. 26, p. 262105, 2010.
- [127] P. Xiao, L. Lan, T. Dong, Z. Lin, W. Shi, R. Yao, X. Zhu, and J. Peng, “InGaZnO thin-film transistors with back channel modification by organic self-assembled monolayers,” *Appl. Phys. Lett.*, vol. 104, no. 5, p. 51607, Feb. 2014.

- [128] P. Xiao, L. Lan, T. Dong, Z. Lin, S. Sun, W. Song, and J. Peng, "InGaZnO Thin-Film Transistors Modified by Self-Assembled Monolayer With Different Alkyl Chain Length," *IEEE Electron Device Lett.*, vol. 36, no. 7, pp. 687–689, Jul. 2015.
- [129] M. Chockalingam, N. Darwish, G. Le Saux, and J. J. Gooding, "Importance of the Indium Tin Oxide Substrate on the Quality of Self-Assembled Monolayers Formed from Organophosphonic Acids," *Langmuir*, vol. 27, no. 6, pp. 2545–2552, Mar. 2011.
- [130] X. Chen, E. Luais, N. Darwish, S. Ciampi, P. Thordarson, and J. J. Gooding, "Studies on the Effect of Solvents on Self-Assembled Monolayers Formed from Organophosphonic Acids on Indium Tin Oxide," *Langmuir*, vol. 28, no. 25, pp. 9487–9495, Jun. 2012.